

Biallelic variants in *HMGCS1* are a novel cause of rare rigid spine syndrome

Lein NH Dofash^{1†}, Lee B Miles^{2†}, Yoshihiko Saito³, Eloy Rivas⁴, Vanessa Calcinotto², Sara Oveissi², Rita J Serrano², Rachel Templin⁵, Georg Ramm⁵, Alison Rodger⁶, Joel Haywood⁷, Evan Ingley¹, Joshua S Clayton¹, Rhonda L Taylor¹, Chiara L Folland¹, David Groth⁸, Daniella H Hock⁹, David A Stroud⁹, Svetlana Gorokhova¹⁰, Sandra Donkervoort¹¹, Carsten G Bönnemann¹¹, Malika Sud¹², Grace VanNoy¹², Brian E Mangilog¹², Lynn Pais¹², Marcos Madruga-Garrido¹³, Marcello Scala¹⁴, Chiara Fiorillo¹⁵, Serena Baratto¹⁶, Monica Traverso¹⁷, Claudio Bruno¹⁸, Federico Zara¹⁴, Carmen Paradas^{19,20}, Katsuhisa Ogata²¹, Ichizo Nishino³, Nigel G Laing¹, Robert J Bryson-Richardson², Macarena Cabrera-Serrano^{20,22,*} and Gianina Ravenscroft^{1*}.

†These authors contributed equally to this work.

Affiliations

¹Harry Perkins Institute of Medical Research, Centre for Medical Research, University of Western Australia, Nedlands, WA 6009, Australia

²School of Biological Sciences, Monash University, Melbourne, VIC, Australia

³Department of Neuromuscular Research, National Institute of Neuroscience, National Center of Neurology and Psychiatry, Kodaira, Tokyo, Japan.

⁴Department of Pathology, Hospital Universitario Virgen del Rocío Sevilla. Spain.

⁵Ramaciotti Centre for Cryo Electron Microscopy, Monash University, Clayton, VIC 3800, Australia

⁶School of Natural Sciences, Macquarie University, Sydney, NSW Australia.

⁷Centre for Crop and Disease Management, School of Molecular and Life Sciences, Curtin University, Bentley, Perth, WA, 6102, Australia

⁸Curtin Medical School, Curtin University; Curtin Health Innovation Research Institute, Curtin University, Bentley, WA, Australia

⁹Department of Biochemistry and Pharmacology, Bio21 Molecular Science and Biotechnology Institute, University of Melbourne, Melbourne, VIC, Australia; Murdoch Children's Research Institute, Royal Children's Hospital, Melbourne, Victoria, Australia; Victorian Clinical Genetics Services, Murdoch Children's Research Institute, Melbourne, VIC, Australia.

NOTE: This preprint reports new research that has not been certified by peer review and should not be used to guide clinical practice.

¹⁰Marseille Medical Genetics Université, INSERM, U 1251, Aix-Marseille Université, 13005 Marseille, France; Department of Medical Genetics, Hôpital Timone Enfants, APHM, 13385 Marseille, France.

¹¹Neuromuscular and Neurogenetic Disorders of Childhood Section, Neurogenetics Branch, NINDS, NIH, Bethesda, MD, USA.

¹²Center for Mendelian Genomics, Broad Institute of MIT and Harvard, Cambridge, Massachusetts, USA.

¹³Hospital Viamed Santa Ángela De la Cruz, Sevilla, 41014, Spain

¹⁴Department of Neurosciences, Rehabilitation, Ophthalmology, Genetics, Maternal and Child Health, University of Genova, Genoa, Italy; Medical Genetics Unit, IRCCS Istituto Giannina Gaslini, Genoa, Italy

¹⁵Child Neuropsychiatry Unit, IRCCS Istituto Giannina Gaslini; Department of Neurosciences, Rehabilitation, Ophthalmology, Genetics, Maternal and Child Health, University of Genova, Genoa, Italy

¹⁶Center of Translational and Experimental Myology, IRCCS Istituto Giannina Gaslini, Genoa, Italy

¹⁷Pediatric Neurology and Muscle Disease Unit, IRCCS Istituto Giannina Gaslini, Genoa, Italy

¹⁸Paediatric Neurology and Neuromuscular Disorders Unit, IRCCS Istituto Giannina Gaslini; Department of Neurosciences, Rehabilitation, Ophthalmology, Genetics, Maternal and Child Health, University of Genova, Genoa, Italy.

¹⁹Department of Neurology, Neuromuscular Unit and Instituto de Biomedicina de Sevilla/CSIC, Hospital Universitario Virgen del Rocío, Sevilla, Spain

²⁰Centro Investigación Biomédica en Red Enfermedades Neurodegenerativas (CIBERNED). Instituto de Salud Carlos III. Sevilla, Spain

²¹Department of Neurology, National Hospital Organization Higashisaitama National Hospital, Hasuda, Saitama, Japan.

²²Department of Neurology, Neuromuscular Unit and Instituto de Biomedicina de Sevilla/CSIC, Hospital Universitario Virgen del Rocío, Sevilla, Spain

***Correspondence to:**

Macarena Cabrera-Serrano

Department of Neurology. Hospital Universitario Virgen del Rocío. Av. Manuel Siurot sn. 41013, Sevilla, Spain.

macabrera@us.es

Gianina Ravenscroft

Harry Perkins Institute of Medical Research. 6 Verdun Street. Nedlands, WA, 6009,
Australia.

gina.ravenscroft@perkins.uwa.edu.au

Running title: HMGCS1 and rigid spine myopathy

Keywords: rigid spine myopathy; HMGCS1; mevalonate pathway; enzymopathy;
neuromuscular disease.

Abbreviations: AcAc-CoA = acetoacetyl coenzyme A; Ac-CoA = acetyl coenzyme A; CD= circular dichroism; HMG-CoA = 3-hydroxy-3-methylglutaryl coenzyme A; K_m = Michaelis constant; MRI= magnetic resonance imaging; TPM = transcripts per million; V_{max} = maximum velocity; WES= whole exome sequencing; WGS= whole genome sequencing

Abstract

Rigid spine syndrome is a rare childhood-onset myopathy characterised by slowly progressive or non-progressive scoliosis, neck and spine contractures, hypotonia, and respiratory insufficiency. Biallelic variants in *SELENON* account for most cases of rigid spine syndrome, however, the underlying genetic cause in some patients remains unexplained.

In this study, we used exome and genome sequencing to investigate the genetic basis of rigid spine syndrome in patients without a genetic diagnosis. In five patients from four unrelated families, we identified biallelic variants in *HMGCS1* (3-hydroxy-3-methylglutaryl-coenzyme A synthase). These included six missense variants and one frameshift variant distributed throughout *HMGCS1*. All patients presented with spinal rigidity primarily affecting the cervical and dorsolumbar regions, scoliosis, and respiratory insufficiency. Creatine kinase levels were variably elevated. The clinical course worsened with intercurrent disease or certain drugs in some patients; one patient died from respiratory failure following infection. Muscle biopsies revealed irregularities in oxidative enzyme staining with occasional internal nuclei and rimmed vacuoles.

HMGCS1 encodes a key enzyme of the mevalonate pathway, disturbance of which is also associated with *HMGCR*-limb girdle muscular dystrophy and *GGPS1*-muscular dystrophy. Quantitative PCR and western blotting confirmed HMGCS1 abundance in skeletal muscle and myogenic precursors. HMGCS1 levels in skeletal muscle were comparable between healthy controls and the index case with a homozygous p.(S447P) substitution. Muscle RNA-seq for a patient with a frameshift variant (c.344_345del:p.S115Wfs*12) and an in trans substitution (p.(Q29L)) showed *HMGCS1* transcript levels reduced to 53% compared to controls. The substitution appeared homozygous on RNA-seq, suggesting the allele harbouring the frameshift variant undergoes nonsense mediated decay.

hmgcs1^{-/-} zebrafish displayed severe early defects, including immobility at 2 days and death by days 3 post-fertilisation. We anticipate that the variants observed in this cohort have subtle effects on HMGCS1 function given most patients survived to adulthood. In support of the variants being hypomorphic, analyses of recombinant human HMGCS1 protein and four mutants (p.S447P, p.Q29L, p.M70T, p.C268S) showed all mutants maintained their secondary structure and dimerized state and had enzymatic activity comparable to the wildtype. Thermal stability of the mutants was similar or slightly reduced compared to the wildtype. Altogether,

our analyses suggest that the identified missense variants in *HMGCS1* act through a hypomorphic mechanism yet to be elucidated.

Here, we report an additional component of the mevalonate pathway associated with myopathy and suggest biallelic variants in *HMGCS1* should be considered in patients presenting with an unresolved rigid spine phenotype.

Introduction

Inherited myopathies are a clinically and genetically heterogeneous group of debilitating disorders characterised by skeletal muscle dysfunction and weakness.¹ Traditional subgroups include congenital myopathies, muscular dystrophies, mitochondrial myopathies, and metabolic myopathies. However, the clinical overlap between these entities can make it difficult to attain an accurate diagnosis.^{1,2}

Rigid spine syndrome is a distinctive manifestation seen in various myopathies.³⁻⁵ Key features include contractures of the limb and spinal joints, limitation of flexion of the neck and trunk, weakness of the cervical and dorsolumbar spine muscles, and progressive scoliosis.³⁻¹⁰ Muscle pathology is variable and can include multiminicores, central cores, rods, rimmed vacuoles, and fibre-type predominance.^{3,4,11} The syndrome typically manifests during the first decade of life. It may be severe, slowly progressive, or non-progressive and may be accompanied by elevated serum creatine kinase levels.² Patients may be susceptible to recurrent infections and respiratory insufficiency which can be fatal.^{3,6-10} For the purposes of this manuscript, the term rigid spine syndrome will be used as an umbrella description for disorders associated with the rigid spine features described above.

The genetic mechanisms and pathways that underlie rigid spine syndrome are diverse.^{5,7,10,14,15} Biallelic variants in *SELENON* encoding selenoprotein N are the most frequently reported cause of rigid spine manifestations.^{8,10,12} Other associated genes include *RYR1*¹⁶, *TOR1AIP1*⁷, *TPM3*¹⁷, *ACTA1*⁹, *TTN*¹⁸, *FHL1*¹⁹, and more recently, *GGPS1*.¹¹ However, the genetic cause in some patients remains unknown despite screening known disease-associated genes.¹³ This suggests that additional genes are yet to be associated with rigid spine syndrome.

In this study, we investigated the genetic cause of rigid spine syndrome in patients remaining without a genetic diagnosis, using exome or genome sequencing and functional genomic approaches. In five patients from four unrelated families, we identified biallelic variants in *HMGCS1*, a gene of the mevalonate pathway encoding 3-hydroxy-3-methylglutaryl-coenzyme A synthase. To our knowledge, *HMGCS1* has not been previously associated with disease, though overlapping myopathic manifestations have been associated with both acquired and inherited disorders of the mevalonate pathway.^{11,20,21} Here, we report biallelic variants in *HMGCS1* as a novel cause of rigid spine syndrome which we have termed *HMGCS1*-myopathy. This report expands the associations of the mevalonate pathway with inherited

skeletal muscle disease and encourages screening of *HMGCS1* in patients with unsolved rigid spine myopathy.

Materials and methods

All investigations were approved by the Human Research Ethics Committee of the recruiting centres (University of Western Australia Human Research Ethics Office, National Center of Neurology and Psychiatry in Japan Human Research Ethics Office, Gaslini Children's Hospital (Comitato Etico della Regione Liguria (163/2018), and the Mass General Brigham Institutional Review Board (Protocol #:2016P001422)). All families participating in this study provided informed consent. Zebrafish experiments and maintenance were approved by Monash Animal Research Precinct 3 committee.

Clinical investigations

Patient details

We have clinically characterised five patients from four unrelated families originating from European or Asian descent. Patients presented with early onset rigid spine syndrome. Serum CK levels were measured in all patients including during acute episodes following intercurrent disease in some patients. Patients were also evaluated for pulmonary function and cardiac involvement. Muscle MRI was performed in some cases. Genomic DNA was isolated from peripheral blood of the patients and their relatives, where available.

Muscle pathology

Muscle biopsies were obtained from some patients as part of routine diagnostic investigations. The samples were frozen and processed for routine histological and histochemical analyses as outlined previously.²²

Genetic investigations

SPAI

Whole exome sequencing (WES) was performed on the affected siblings (patients P1 and P2) and their unaffected parents at the Center for Mendelian Genomics (Broad Institute of Harvard and MIT, Boston, USA). Exome capture was accomplished using an Illumina 37 Mb exome target (150 bp paired reads). Variant curation was performed in seqr (<https://seqr.broadinstitute.org/>).²³ Variants were filtered based on a presumed autosomal recessive mode of inheritance and were restricted to rare (frequency<0.01 in gnomAD) coding variants, including extended splice-site variants. The *HMGC1* variant was confirmed by PCR and bi-directional Sanger sequencing (Australian Genome Research Facility (AGRF) Perth, Australia).

JPNI

After standard DNA extraction, WES was performed for patient P3, unaffected parents and two unaffected siblings at department of Neuromuscular Research (National Institute of Neuroscience in National Center of Neurology and Psychiatry, Tokyo, Japan). Samples were processed using TruSeq DNA PCR-free sample preparation and 150 bp paired-end sequencing was conducted on the NovaSeq 6000 platform (BGI, China). BWA (0.7.5a-r405, <https://github.com/lh3/bwa>) and Picard (1.141, <https://github.com/broadinstitute/picard/issues/431>) were used to map low-divergent sequences from the human genome reference (GRCh37). GATK 3.5 (<https://gatk.broadinstitute.org/hc/en-us>) was used to call variants. Variants were then annotated with ANNOVAR. The variants were filtered based on a presumed autosomal recessive mode of inheritance and was restricted to rare (frequency<0.01 in gnomAD) coding variants, including extended splice-site variants. Bi-allelic variants in *HMGC1* were confirmed by Sanger sequencing of the parents.

ITAI

After standard DNA extraction, trio WES was performed for patient P4 and their unaffected parents as previously described.²⁴ The selection of the coding regions and flanking intronic sequences was made using the enrichment kit IDT xGen Exome Research Panel v2 (34 Mb, 19,433 geni). The sequencing was performed using Illumina technologies (PE 2X150) with the

platform Illumina Novaseq6000. The quality of the sequence reads was assessed through QC statistics with FastQC (<http://www.bioinformatics.bbsrc.ac.uk/projects/fastqc>). Reads were aligned to the reference human genome (hg38, UCSC assembly) using BWA with default parameters. The HaplotypeCaller algorithm within the Genome Analysis Toolkit (GATK) package was employed for quality score recalibration, indel realignment, and variant calling. Variants were then annotated with ANNOVAR. After filtering for variants with a minor allele frequency (MAF) ≤ 0.001 in gnomAD (<https://gnomad.broadinstitute.org>) and an in-house database of 6,500 exomes, the predicted impact of the candidate variants on protein structure and function was evaluated through *in silico* prediction tools.

USA1

Whole genome sequencing and data processing were performed by the Genomics Platform at the Broad Institute of MIT and Harvard. PCR-free preparation of sample DNA (350 ng input at >2 ng/ul) was conducted using Illumina HiSeq X Ten v2 chemistry. Libraries were sequenced to a mean target coverage of $>30x$. Genome sequencing data was processed through a pipeline based on Picard, using base quality score recalibration and local realignment at known indels. Reads were mapped to the hg38 using BWA aligner. Single nucleotide variants (SNVs) and insertions/deletions (indels) were jointly called across all samples using the GATK HaplotypeCaller package version 4.0. Default filters were applied to SNV and indel calls using the GATK Variant Quality Score Recalibration (VQSR) approach. Annotation was performed using Variant Effect Predictor (VEP). Lastly, the variant call set was uploaded to seqr for collaborative analysis between the Centers for Mendelian Genomics (CMG) and investigator.

Analysis of the HMGCS1 substitutions

Positions of the *HMGCS1* substitutions were annotated on the *HMGCS1* gene (ENSG00000112972) and protein structure (PDB: 2P8U).²⁵ The crystal structure for HMGCS1 was accessed from the Protein Data Bank (PDB; www.rcsb.org)²⁶ and analysed using the PyMOL Molecular Graphics System, Version 2.4.1. Annotations including residues of the HMGCS1 active sites, CoA binding sites, and the salt bridge were obtained from the UniProt database (Q01581) and the ICn3D (I-see-in-3D) molecular structure viewer.²⁷ For conservation analysis, HMGCS1 amino acid sequences were obtained from UniProt and aligned by Clustal omega alignment (<https://www.ebi.ac.uk/Tools/msa/clustalo/>).

***HMGCS1* expression**

Gene expression databases

Bulk RNA-seq data for *HMGCS1* (ENST00000325110) was obtained from the Genotype-Tissue Expression (GTEx) portal (<https://gtexportal.org/>) and NCBI (BioProject PRJEB4337). Cap Analysis Gene Expression (CAGE) data was obtained from the Functional Annotation of the Mammalian genome consortium (FANTOM5; <https://fantom.gsc.riken.jp/5/>).²⁸

RNA sequencing

Skeletal muscle RNA-seq was performed for patient P3 (JPN1) and three unaffected control samples from the National Center of Neurology and Psychiatry. RNA was extracted with the RNeasy Plus Mini Kit (Qiagen, Valencia, CA, USA; 74136). Libraries were prepared from total RNA with a TruSeq Stranded Total RNA Library Prep Kit (polyA capture, Illumina), according to the manufacturer's instructions, and 100 bp paired-end sequencing conducted on the NovaSeq 6000 platform; 8 Gb of sequence data encompassing *HMGCS1* were generated for each sample (Macrogen, Seoul, Korea). RNA-seq reads were mapped using Spliced Transcripts Alignments to Reference (STAR) software (<https://github.com/alexdobin/STAR>). The reads were processed using StrandNGS® v4.0 (<http://www.strand-ngs.com/>) and analysed by DESeq²⁹ compared to the three unaffected control samples.

We used DROP v1.0.3³⁰, as previously described³¹, to analyse aberrant gene expression amongst a cohort of 129 skeletal muscle RNA-seq from rare muscle disease patients and unaffected controls, including JPN1. DROP leverages OUTRIDER³², which uses a denoising autoencoder to control co-variation before fitting each gene over all samples via negative binomial distribution. Multiple testing correction was done across all genes per sample using DROP's in-built Benjamini-Yekutieli's false discovery rate (FDR) method.

Quantitative PCR

Quantitative real-time PCR (qPCR) was performed to investigate *HMGCS1* transcript levels in healthy human tissue and cell lines. RNA extraction, cDNA synthesis and qPCR were performed as previously described.³³ Reactions (10 µL) were performed using 2X Rotor-Gene SYBR Green PCR master mix (Qiagen; 204076) and contained 1 µL diluted cDNA and 0.8

μM of forward and reverse primers (5'-TTCCCTTGCATCTGTTCTAGC-3' and 5'-TTTTATCAAGAGCAGACCCCG-3'). Reactions were performed for biological replicates depending on availability of samples ($n=2-7$). Cycling was performed on a Rotor-Gene Q real-time PCR cycler (Qiagen) as follows: 95°C (5 min), 45 cycles of 95°C (10 s) and 60°C (15 s), and subsequent melt curve analysis (60- 95°C; +1°C per cycle). Data were normalised using the delta Ct method³⁴ by comparing to the geometric mean of two reference genes (*TBP* and *EEF2*).³⁵

HMGCS1 protein abundance

Western blotting

Protein extraction and western blotting were performed as previously described.³⁶ Frozen cell pellets and shredded tissue were suspended in lysis buffer containing 2% SDS, 125 mM Tris (pH 6.8), and 1x PIC (Halt™ Protease Inhibitor Cocktail; Thermo Scientific) and homogenised by sonication. Protein concentrations were determined by a BCA protein assay (Pierce; #23227). Samples were prepared in loading buffer (10% SDS, 312.5 mM Tris (pH 6.8), 50% glycerol, bromophenol blue saturated solution, 50 mM DTT and 1x PIC). Extracts (12 μg) and recombinant HMGCS1 (5 ng; production described below) were separated on 4-12% Bis-Tris NuPAGE Novex polyacrylamide gels and transferred to PVDF transfer membranes (Thermo Fisher Scientific). Membranes were blocked with PBS + 0.1% Tween-20 and 5% skim milk for 1 h at room temperature (RT) and probed with an anti-HMGCS1 rabbit polyclonal antibody (MyBioSource; #MBS2026097; 1:800 incubated overnight at 4°C) and subsequently, a secondary goat anti-rabbit horseradish peroxidase antibody (Sigma; #A0545) for 1 h at RT. Membranes were imaged by chemiluminescent detection (Pierce ECL Plus kit; #32132) using the Invitrogen iBright FL1000 imaging system (Thermo Fisher Scientific). An anti-GAPDH antibody (Sigma; #G8795; 1:10,000) was used as a loading control. Relative HMGCS1 abundance was calculated using ImageJ.³⁷

Identification of HMGCS1 in primary human myoblasts and myotubes by mass spectrometry

Myoblasts and myotubes (day 2 and day 8 of terminal differentiation) from three healthy human donors (18M [P01236-18M], 32F [P01034-32F] and 42F [P01269-42F]; Cook

Myosite)³⁸ were solubilised in 5% sodium dodecyl sulphate (SDS), 50mM tetraethylammonium bromide (TEAB) and sonicated with a probe sonicator for 10 s on/off cycles for 30 s on ice. Samples were quantified via bicinchoninic acid (BCA) protein assay (Thermo Fischer Scientific), normalised to 60 ug of total protein and prepared for liquid chromatography tandem mass spectrometry (LC-MS/MS) using micro S-trapTM columns (ProtiFi) as per manufacturer's protocol. Protein reduction and alkylation were performed with 40 mM 2-chloroacetamide (CAA) and 10 mM tris(2-carboxyethyl)phosphine hydrochloride (TCEP) at 99°C for 5 min with 1500 rpm shaking. Proteins were digested at 1:25 trypsin:protein ratio overnight. LC-MS/MS data was acquired as previously.³⁹ Raw data were processed using the Spectronaut platform (version 14, Biognosys) and searched against the UniProt human database (canonical peptides and isoforms, reviewed, 42,386 entries) and a peptide library containing 147,852 entries. Default settings were used with exception of single hit proteins were excluded from the data and precursors were filtered on Q-value with imputation strategy set to "none". Number of peptides were plotted with GraphPad Prism 9.0.1 (La Jolla, USA).

Functional genomic investigations

Recombinant protein expression

Bacterial pET-30a(+) expression constructs were synthesised by Genscript (<https://www.genscript.com/>). These encoded the coding DNA sequences for wildtype human HMGCS1 (ENST00000325110, HMGCS1^{WT}), and mutants encoding one of the four missense variants: p.Ser447Pro (HMGCS1^{S447P}), p.Gln29Leu (HMGCS1^{Q29L}), p.Met70Thr (HMGCS1^{M70T}), or p.Cys268Ser (HMGCS1^{C268S}) identified in patients. The constructs were codon-optimised for *E. coli* expression and included a six-histidine tag at the N-terminus. Constructs were transformed into BL21-DE3 *E. coli* following a standard heat-shock method.⁴⁰ Cultures were grown at 37°C in Luria-Bertani (LB) broth containing 35 µg/mL kanamycin. Expression was induced with 0.1 mM Isopropyl β-d-1-thiogalactopyranoside (IPTG) with overnight growth at 16°C. Protein extraction and purification were performed as previously described.⁴¹ Cultures were lysed by sonication in 50 mM Tris (pH 8.0), 250 mM sodium chloride, 10% v/v glycerol and 0.1% Triton X-100. The soluble fraction containing recombinant protein was incubated overnight at 4°C with resins (profinity IMAC, #156-0123)

charged with 0.2 M Nickel (II) sulfate hexahydrate (Sigma). Proteins were eluted by washing in buffer containing 50 mM Tris (pH 8.0), 150 mM NaCl, and 5% glycerol and increasing concentrations of imidazole (0 to 300 mM). Eluants were concentrated to in buffer containing 50 mM Tris (pH 8.14), 150 mM NaCl and 5% glycerol by centrifuging at 3,000 g, 4°C using 30 kDa Amicon ultra centrifugal filter units (Sigma).

Size exclusion chromatography

Size exclusion chromatography was performed as previously described.⁴¹ Protein concentrates were loaded onto a XK16/600 Superdex 200 column (GE Healthcare Life Sciences) for purification. Columns were equilibrated in 150 mM NaCl, 50 mM Tris (pH 8.14), 10% v/v glycerol. Fractions were collected and tested for protein of the expected size by SDS-PAGE. Protein identity and purity were determined by mass spectrophotometry (Proteomics International, Perth). The concentration of recombinant protein was determined using a NanoDrop 2000 V1.5 (Thermo Scientific) at 280 nm. The exclusion coefficient and molecular weight of protein were calculated using the ExPASy ProtParam webtool (<https://web.expasy.org/protparam/>).⁴² The extinction coefficient and molecular weight (excluding His-tags) for HMGCS1 was 65.39 mM⁻¹cm⁻¹ and 57.29 kDa, respectively.

Circular dichroism

For circular dichroism (CD) melting curve and spectra analyses, recombinant wildtype and mutant HMGCS1 were diluted to 0.1 mg/mL in 10 mM sodium phosphate buffer (pH 7.4). In technical replicates, 300 µL of protein and buffer were loaded into 0.1 cm quartz cuvettes and measured by a Jasco J-1500 CD spectropolarimeter. For the melting curves, samples were measured at temperatures ranging between 15–95°C at 220 nm and 229 nm at a rate of +0.25°C/min (30 s data integration time [DIT], 2.00 nm bandwidth). Throughout the melting curve process (approx. every 5°C), CD spectra were measured between 195–260 nm (0.2 nm data pitch, 4 s DIT, 2.00 nm bandwidth). Data were collected using the JASCO Spectra manager software (2.15.24). Cuvette baseline measurements were subtracted from the sample spectra measurements. Data were zeroed by subtracting the average signal between 250–260 nm. Melt curves were generated using GraphPad Prism 9.0.1 (La Jolla, USA) by fitting each dataset to a sigmoidal four parameter logistic regression curve. The fits generated for each melt curve were based on temperature ranges which best captured protein folding in that particular dataset. The half height value was taken as a measure of protein melting temperature (T_m ;

temperature at which 50% of protein is denatured). Data were analysed by a one-way ANOVA followed by Dunnet's multiple comparison test and paired t-test to measure statistical significance using GraphPad Prism 9.0.1 (La Jolla, USA).

Enzyme assays

HMGCS1 catalyses the condensation reaction between acetyl coenzyme A (Ac-CoA) and acetoacetyl coenzyme A (AcAc-CoA) to form 3-hydroxy-3-methylglutaryl coenzyme A (HMG-CoA).⁴³ To investigate the effect of the missense substitutions on HMGCS1 activity, we adapted an assay described by Lowe and Tubbs (1985)⁴³ which measures the decrease in absorbance (303 nm) as AcAc-CoA is consumed. The standard assay system contained 100 mM Tris/HCl (pH 8.0) and 40 mM MgCl₂ in a total volume of 200 µl. Reactions were performed in triplicate in a UV-star 96 well microplate (Greiner) at 25°C and initiated with 1 µg of enzyme or with buffer alone as a no enzyme control (NEC). Concentrations of Ac-CoA and AcAc-CoA ranged between 0-300 µM. The amount of AcAc-CoA consumed per reaction was determined in relation to a standard curve and reactions were fit to non-linear one phase decay plots using GraphPad Prism 9.0.1 (La Jolla, USA). The amount of AcAc-CoA consumed within the first 50 s of the reactions was taken as a measure of the initial velocity (V₀).

Generation of zebrafish *hmgcs1* mutant line

The zebrafish *hmgcs1* null mutant line was generated by injecting one-cell stage embryos with a mix containing two pre-complexed guideRNA's (Integrated DNA Technologies, Alt-R™) targeting exon3 (GCTTGGTCAACGTAAGTGGAGAtgg and GACACCACTAACGCCTGCTAtgg), Cas9 protein (HiFi v3 from Integrated DNA Technologies), 300 mM KCl, and 0.005% phenol red. Injected embryos were raised to adulthood and crossed to wildtype fish, and embryos screened for deletions using the following genotyping primers: *hmgcs1_ex3_F* CCATGTGGCCCAAAGATGTG, *hmgcs1_ex3_R* TGGACTCCACCCAGTTGAC. A founder passing on a 302 bp deletion in exon3 was identified.

HMGCS1 rescue experiments

Human wildtype HMGCS1 was codon-optimised for zebrafish using CodonZ⁴⁴ and synthesised with an Sp6 transcriptional start site and an *afp* 3'UTR by Genscript™. Capped mRNA for injection was synthesised using the mMessage mMachine Sp6 kit (ThermoFisher

Scientific). One-cell stage embryos from *hmgcs1* heterozygote incrosses were injected with a mix containing HMGCS1 mRNA at 18 ng/ul, 300 mM KCl, 0.005% Phenol red, and cascade blue labelled dextran (Molecular Probes). Control-injection mix did not contain mRNA. Embryo survival was recorded daily until 4 days post-fertilisation. Remaining embryos were genotyped to determine the number of homozygous mutants alive.

Electron microscopy

48 h post-fertilisation embryos were fixed in 0.1 M sodium cacodylate buffer containing 2% paraformaldehyde and 2.5% glutaraldehyde for 24 h and rinsed with 0.1 M sodium cacodylate buffer (3x 10 min). Embryos were genotyped prior to processing. Samples were processed using a method modified from Hua, Laserstein, Helmstaedter.⁴⁵ All processing steps were aided by a microwave regime (Pelco Biowave) and performed at room temperature unless otherwise stated. Samples were post-fixed in 2% osmium tetroxide in 0.1 M sodium cacodylate buffer for 12 min (2 min on/off cycles, 150 W, under vacuum) which was reduced with 1.5% potassium ferrocyanide in 0.1M sodium cacodylate for 12 min (2 min on/off cycles, 150 W, under vacuum). Samples were thoroughly rinsed in MilliQ (mQ) H₂O for 3 x 40 s (150 W, no vacuum). This was followed with 1% aqueous thiocarbohydrazide solution for 12 min at 50°C (2 min on/off cycles, 150 W, under vacuum) and again rinsed thoroughly in mQH₂O (3x 40 s, 150 W, no vacuum). Samples underwent further osmification in 2% osmium tetroxide (aqueous) for 12 min (2 min on/off cycles, 150 W, under vacuum), at room temperature. After rinsing with mQH₂O as previous, samples were exchanged into 1% uranyl acetate (aqueous) overnight at 4°C. The following day the temperature was increased to 50°C in the biowave for further processing for 12 min (2 min on/off cycles, 150 W, under vacuum). Samples were again rinsed with mQH₂O as previous. The final staining step involved incubation in lead aspartate for 12 min at 50°C (2 min on/off cycles, 150 W, under vacuum) and rinsing in mQH₂O (as previous). Samples were then dehydrated with increasing concentrations of ethanol before final dehydration with acetone (ethanol: 20%, 50%, 70%, 90%, 2 x 100%; acetone: 2 x 100%) for 40 s per step (150 W, no vacuum), and infiltrated with increasing concentrations of hard EPON resin in acetone for 3 min each step (25%, 50%, and 75%, 2 x 100%). Samples were left in fresh 100% resin overnight. After being transferred into a silicone mould, samples were polymerised into blocks in the oven at 60°C for 48 h.

Longitudinal sections were cut at 70 nm on a ultramicrotome (Leica UC7) and collected on copper mesh grids. Samples were imaged on a Fei Nova Nano SEM 450 using the STEM2

detector at 30 kV. Maps software package (Thermo Fisher) was used to automatically acquire tiled regions with a pixel size of 6 nm. Tiles were assembled using the deprecated Stitch Grid of Images plugin within Fiji.⁴⁶

Mitochondrial quantification in electron microscopy images

The number of mitochondria within a randomly sampled somite were quantified in *hmgcs1*^{+/+} and *hmgcs1*^{-/-} using the Multipoint tool in Fiji.⁴⁶ Abnormal mitochondria were scored as showing detachment or invagination of the inner membrane and expressed as the percentage of the number of abnormal mitochondria/total number of mitochondria. Somite area was quantified by drawing a rectangle around the somite using the polygon tool in Fiji and used to normalize the number of mitochondria for each sample. The researcher was blinded to the genotype and the order of images randomised, during mitochondria scoring and area measurement, with the genotypes revealed for statistical comparison conducted by another researcher.

Data availability

The data and constructs generated by this study are available upon request.

Results

Clinical findings

We report five patients from four families presenting with a clinical picture of rigid spine syndrome (Fig 1, Table 1 and Supplementary material). Age-of-onset ranged from birth to childhood. There was no relevant family history of disease in any of the families. Features included spinal rigidity primarily affecting the cervical ($n=5/5$) and dorsolumbar ($n=4/5$) regions, and scoliosis ($n=5/5$). All patients had restrictive pulmonary function with a forced vital capacity ranging between 10-56%. Some patients also presented with weakness of the proximal ($n=4/5$) and distal ($n=2/5$) limbs, scapular winging ($n=3/5$), and bulbar weakness ($n=1/5$; Table 1). None of the patients presented with facial weakness, ophthalmoparesis, or ptosis. Baseline creatine kinase levels were variably elevated in all cases, ranging between 190-7890 IU/L (normal ~70-170 IU/L⁴⁷). In three patients (P1, P3, P5) episodes of muscle

deterioration and respiratory crisis were triggered by intercurrent disease or certain drugs. Patient P2 (SPA1) died during their teenage years from such an episode after developing a respiratory infection followed by a rapid decline in muscle strength and respiratory function leading to respiratory failure. Patient P3 (JPN1) was also reported to experience such episodes and elevated creatine kinase levels during febrile illness. The episode of decline for patient P5 (USA1) was triggered after starting megestrol and slowly improved after discontinuing the drug.

Muscle MRI performed for two of five patients (P1, P4) showed variability in T1 signaling primarily in the posterior muscles of the hip, thigh, and leg (Fig 2A). Muscle MRI of patient P1 (SPA1) indicated extensive fatty replacement in the cervical paraspinal muscles (Fig 2Ai) as well as involvement of the posterior compartment of the thighs (Fig 2Aii). Edema was also observed in the posterior compartment of the thighs on STIR (Short Tau Inversion Recovery) imaging of patient P1 (Fig 2Aiii). Lower leg muscle MRI of patient P1 was normal (not shown). Muscle MRI of patient P4 (ITA1) similarly indicated fatty infiltration in the posterior compartment of the thighs (Fig 2Aiv,v) as well as in the posterior compartment of the leg (Fig 2Avi).

Four patients (P1, P3, P4, P5) underwent muscle biopsy. The most noticeable findings were irregularities on oxidative enzyme staining, including core-like regions in some myofibres as shown by SDH and NADH staining (Fig 2B). There were also occasional internal nuclei and rimmed vacuoles observed on H&E and Gömöri Trichrome staining (Fig 2B) in some patients. The muscle pathology of patient P3 worsened with age, showing the presence of rimmed vacuoles and dystrophic features during adulthood which were absent during childhood (Fig 2B). Muscle biopsy for patient P5 was indicative of a chronic myopathy with marked macrophage infiltration. There were also vacuoles and atrophic myofibres present (images unavailable).

Genetic investigations

We identified seven novel or rare biallelic variants in *HMGCS1* (ENSG00000112972) cosegregating with rigid spine syndrome in four families (Fig 1A, Fig 3A). This included six missense variants and one frameshift variant. In the index family (SPA1), we identified a homozygous missense variant in *HMGCS1*, c.1339T>C, p.(Ser447Pro) in the two affected

siblings (P1, P2). The variant was absent in gnomAD data (v2.1.1) and was heterozygous in the unaffected parents as confirmed by Sanger sequencing. Additional rigid spine syndrome cases with biallelic *HMGCS1* variants were subsequently identified via international collaborations and gene-matching platforms, including the Broad Institute's matchbox. In JPN1, exome data for patient P3 revealed a maternally inherited missense variant (c.86A>T, p.(Gln29Leu)) in trans with a paternally inherited frameshift variant (c.344_345del, p.(S115Wfs*12)). The two unaffected siblings were identified as carriers for the frameshift variant (Fig 1A). In ITA1, the affected proband (P4) was identified with compound heterozygous missense variants (c.890G>T, p.(Gly297Val) maternal allele, in trans with c.1289G>A, p.(Arg430Lys), paternal allele). In USA1, patient P5 had compound heterozygous missense variants: c.209T>C, p.(Met70Thr), maternal allele, in trans with c.803G>C, p.(Cys268Ser), paternal allele. All variants identified in this cohort were absent from gnomAD except for the c.803G>C, p.(Cys268Ser) variant, which was present in the heterozygous state in 4 of 251,086 alleles (all from the European non-Finnish population, frequency 1.59×10^{-5}). Apart from the M70 residue, all substituted residues in this cohort are conserved in multiple species as well as in human *HMGCS2*, the mitochondrial paralogue (Fig 3B). Further details including variant effect predictions are included in Supplementary Table 1.

The c.209T>C, p.(Met70Thr) variant was also identified via gene matching in an additional proband (in the USA, Supplementary Table 1, USA2) presenting with a similar unresolved rigid spine phenotype. This variant was heterozygous in the proband and inherited from the unaffected father. However, whole genome sequencing and RNA-seq of patient fibroblasts did not identify a second likely pathogenic *HMGCS1* variant in trans for this patient suggesting a possible more complex underlying genetic cause such as a genomic rearrangement. Alternatively, it remains inconclusive whether *HMGCS1* is the underlying genetic cause of rigid spine syndrome for this case.

The compound heterozygous frameshift variant (c.344_345del, p.(Ser115Trpfs*12)) in patient P3 (JPN1) was predicted to result in nonsense mediated decay of the transcript. Indeed, RNA-seq of patient muscle showed only one read (out of 44) contained the frameshift variant while all reads (41/41) spanning the c.86 position contained the c.86A>T, p.(Gln29Leu) variant (Fig 3C). In further support, expression analyses via DEseq²⁹ indicated there was a 0.53 fold decrease in *HMGCS1* transcript levels in the patient relative to three controls (Fig 3C). Collectively, this suggests that at a protein level, in patient P3, the c.86A>T, p.(Gln29Leu)

variant is almost exclusively present.

To determine whether HMGCS1 dysfunction is associated with aberrant expression of other genes of the mevalonate pathway, we analysed RNA-seq for patient P3 against 129 individuals by OUTRIDER.³² We identified eight expression outliers in patient P3 (Supplementary Fig 1). However, no candidates showed any remarkable associations with the mevalonate pathway or other shared pathway according to gene ontology enrichment analyses.

Protein studies

The variants identified in the patients were scattered in several exons in *HMGCS1* (Fig 3A). These include exon 3 (p.(Q29L), p.(M70T), p.(S115Wfs*12)), exon 6 (p.(C268S), p.(G297V)), exon 9 (p.(R430K)) and exon 10 (p.(S447P)). The C268S substitution is adjacent to a coenzyme A (CoA) binding residue, K269 (Fig 3A). Positions of the remaining substitutions were distant from residues of the CoA active sites (E95, C129, H264), binding sites (S221, K269, K273) and residues of the dimer salt bridge (D119, Glu121, R194, D208, K239, K461 and H462). Three substituted residues (Q29, M70, and S447) appear to cluster towards the surface of HMGCS1 (Fig 3D). Residues Q29 and S447 appear <5 Å apart in 3D space according to the PDB model (Fig 3D).

HMGCS1 is abundant in various tissues, including developing and adult skeletal muscle

RNA-seq data from the NCBI BioProject (PRJEB4337)⁴⁸ and the GTEx portal⁴⁹ indicated that *HMGCS1* is enriched in brain and liver and is expressed at lower levels in other tissues, including skeletal muscle. Similarly, qPCR analyses indicated enriched expression of *HMGCS1* in human cortex, and relatively lower expression in cells and tissues, including myotubes and adult skeletal muscle (Fig 4A). Of the myogenic samples analysed in the FANTOM5²⁸ database, *HMGCS1* expression was highest in skeletal muscle satellite cells (235-462 transcripts per million (TPM)) relative to fetal-derived skeletal muscle cells (3-326 TPM), myotubes (0-240 TPM), and myoblasts (31-50 TPM).

Western blotting for HMGCS1 in human tissues and cells revealed a band of the expected size (~57 kDa; Fig 4C-F), which matched the product size of the recombinant HMGCS1 protein (Fig 4E). We show that HMGCS1 is enriched in the cortex (Fig 4D), consistent with the qPCR

data and the proteomic data from the Human Protein Atlas⁵⁰. In addition, HMGCS1 was detected in adult human skeletal muscle and was relatively less abundant in human fetal skeletal muscle (Fig 4D), consistent with the qPCR studies. HMGCS1 was also detected in human myoblasts and myotubes from days 0 to 12 of differentiation by mass spectrometry (Fig 4B) and/or western blotting (Fig 4C). There was comparable abundance of HMGCS1 in skeletal muscle of patient P1 (SPA1) and control skeletal muscle biopsies (Fig 4E) suggesting the p.(S447P) substitution does not reduce protein stability or abundance. Similar levels of Hmgcs1 were detected in mouse EDL (*extensor digitorum longus*) and soleus muscles (Fig 4F), suggesting that Hmgcs1 is similarly abundant in fast- and slow-twitch myofibres in mice.

Functional investigations of recombinant HMGCS1

HMGCS1 has been reported to exist as a dimer.^{25,51} To investigate whether substitutions in HMGCS1 affect dimerisation, the recombinant wildtype (HMGCS1^{WT}) and mutant proteins (HMGCS1^{S447P}, HMGCS1^{Q29L}, HMGCS1^{M70T} and HMGCS1^{C268S}) were analysed by size exclusion chromatography to evaluate monomer and dimer content. All proteins eluted at equivalent points corresponding to the expected molecular weight for dimerised HMGCS1 (Supplementary Fig 2A,B). This suggested that the substitutions do not interfere with HMGCS1 dimerisation. There were second peaks detected for HMGCS1^{WT} and HMGCS1^{Q29L} (Supplementary Fig 2A), however, their elution volumes did not correspond to the expected molecular weight of the monomer (Supplementary Fig 2B).

Circular dichroism spectra and melting curve analyses were performed to investigate whether the HMGCS1 variants affected protein structure and thermal stability, respectively. Overall, the wildtype and all mutants investigated appeared structurally stable, showing considerable overlap in the CD spectra (190–260 nm) throughout the melting range (15–95°C; Fig 5A-D). The majority of the protein remained intact even at high temperatures (> 60°C), showing marginal changes in CD signal suggesting the proteins have a thermally stable core (Fig 5E). The melting curves we measured suggested only a small part of the protein unfolded below 95°C. Owing to the relative stability of the proteins, the small changes in CD signal, and the variability between experiments, there were no statistically significant differences in protein stability detected between the mutants and the wildtype (one-way ANOVA, Fig 5F). Though there was a trend suggesting the M70T and C268S mutants may be less stable than the wildtype across the independent experiments (Fig 5F). The WT and p.S447P proteins were run in three

additional experiments in which the p.S447P protein showed a small (2.6°C) decrease in protein stability compared to WT (paired t-test, $n = 7$, $p = 0.03$; Fig 5F).

All mutants also appeared to retain enzymatic activity and showed no significant changes in activity compared to the wildtype when assayed under multiple substrate concentrations (Supplementary Fig 3). This included HMGCS1^{C268S} which, despite harboring a substitution neighboring the CoA binding site, only showed a ~30% reduction in activity relative to the wildtype when assayed with 200 μ M AcAc-CoA and Ac-CoA (Supplementary Fig 3B). However, the small changes in the absorbance and the resulting variability between runs made it difficult to confirm whether any partial changes detected were significant. Nonetheless it was apparent that the substitutions do not drastically impair enzymatic activity.

***hmgcs1* null zebrafish present severe movement defects, mitochondrial abnormalities, and an early lethal phenotype**

To evaluate the effect of loss of HMGCS1 function in an animal model during developmental stages we generated a *hmgcs1* mutant zebrafish, containing a 302 bp deletion in exon 3, which results in a frameshift after 35 aa (Supplementary Figure 5A). Loss of Hmgcs1 in zebrafish embryos results in severe early developmental defects, with *hmgcs1*^{-/-} embryos displaying blood pooling in the brain, reduced pigmentation (Figure 6A), absence of movement at 48 hours post fertilisation (hpf, Fig 6B), and lethality at 3 days post fertilisation (dpf, Fig 6C). Further investigation of the movement defect identified that *hmgcs1*^{-/-} embryos completely lack a touch-evoked escape response⁵² compared to *hmgcs1*^{+/+} and *hmgcs1*^{+/-} siblings.

Injection of mRNA encoding HMGCS1 was able to rescue early lethality in *hmgcs1*^{-/-} embryos (Figure 6C), as well as the movement defects in response to touch (Figure 6B), demonstrating that these defects specifically result from the loss of Hmgcs1 function.

Electron microscopy to investigate the muscle ultra structure revealed that *hmgcs1*^{-/-} embryos exhibited significant mitochondrial abnormalities within the skeletal muscle at 48 hpf, presenting as a detachment or invagination of the inner membrane (Figure 6D,F), without affecting mitochondrial density (Figure 6E). Interestingly, the myofibril pattern in *hmgcs1*^{-/-} animals was indistinguishable from wildtype siblings, indicating that the muscle structure was not affected (Figure 6D, cyan arrows). These results indicate that absence of Hmgcs1 results in damage to the integrity of the mitochondrial membrane and loss of muscle function.

Discussion

We report the identification of seven biallelic variants in *HMGCS1* in four unrelated families with rigid spine syndrome. Although the cohort thus far includes five patients, the distinct rigid spine phenotype shared by the patients, including disease onset and severity suggests a common genetic basis of disease which we define here as *HMGCS1*-related myopathy.

HMGCS1 encodes the cytosolic HMG-CoA synthase; a key enzyme of the mevalonate pathway which catalyses the condensation reaction between AcAc-CoA and Ac-CoA to form HMG-CoA.²⁵ Its mitochondrial paralogue; HMGCS2 catalyses the same reaction for the ketogenesis pathway. Biallelic variants in *HMGCS2* are associated with HMG-CoA synthase deficiency (OMIM# 605911) characterised by episodic metabolic distress, febrile crisis, hepatomegaly, and respiratory distress.⁵³⁻⁵⁵ *HMGCS1* and *HMGCS2* share ~67% sequence similarity and five of the six substituted *HMGCS1* residues presented here (Q29, C268, G297, R430 and S447) are conserved in *HMGCS2* (Q66, C305, G334, R467 and S484, respectively) suggesting that they are of functional importance. Thus far, none of the *HMGCS1* substitutions observed in this study overlap with the reported *HMGCS2* pathogenic substitutions. Nevertheless, the association of biallelic variants in *HMGCS2* with disease suggests that biallelic variants in *HMGCS1* can be similarly deleterious. This is further supported by gnomAD constraint scores which indicate that *HMGCS1* (pLI=1; Z=3.04) is substantially more intolerant to loss-of-function and missense variation compared to *HMGCS2* (pLI=0; Z=-0.19).

Myopathic and rigid spine phenotypes have been associated with several inborn and acquired errors of the mevalonate pathway.^{11,20,21,56-64} This includes biallelic variants in *HMGCR* (HMG-CoA reductase) immediately downstream of *HMGCS1* in the pathway (Supplementary Fig 4), which have recently been associated with limb-girdle muscular dystrophy (OMIM# 620375).^{21,65} Inhibition of *HMGCR* by statins and autoantibodies are also associated with acquired muscle disorders including statin-induced myopathy²⁰ and anti-*HMGCR* myopathy.^{59,61,66,67} Further downstream, inhibition of *FDPS* (farnesyl diphosphate synthase) by bisphosphonate medications has been associated with profound muscle weakness with fever and flu-like symptoms.^{68,69} Moreover, biallelic variants in *GGPS1* have been associated with a muscular dystrophy (OMIM# 619518).^{11,70} Of note, *GGPS1*-related muscular dystrophy includes several overlapping phenotypes including scoliosis, joint contractures, hypotonia, elevated creatine kinase, as well as episodic worsening of muscle weakness and respiratory

insufficiency during intercurrent disease.^{11,70} Overall, the myopathic phenotypes implicated in the mevalonate pathway support *HMGCS1* as an underlying genetic cause for our patients' disorders.¹¹

The mevalonate pathway branches into several critical other pathways including the cholesterol biosynthesis pathway, the isoprenoid pathway and the ubiquinone pathway, which are essential for regulating cell proliferation, maturation, and maintenance.⁷¹ Genes of these pathways, including *HMGCS1* are conserved in eukaryotes, archaea and some bacteria.^{25,71-73} Knockdown of most genes of the mevalonate pathway is associated with complete preweaning lethality in mice (Supplementary Fig 4).^{11,74} Knockdown of *Hmgcs1* in mice is associated with prenatal lethality (International Mouse Phenotyping Consortium, <https://www.mousephenotype.org/data/genes/MGI:107592>), with no homozygous pups observed at E9.5. It is thought that this arises due to placental defects (personal communication, JAX lab). A severe phenotype was similarly observed in our studies of *hmgcs1*^{-/-} zebrafish, which included developmental delay, immobility by 2 dpf, and fatality during 3 dpf. There were also significant mitochondrial abnormalities in the skeletal muscle, which is consistent with mitochondrial changes reported in a *c. elegans* *hmgr-1* mutant.⁷⁵ Pharmacological inhibition of Hmgcr in zebrafish and mouse models is associated with severe multi-system defects despite predominantly being associated with myopathies in humans.⁷⁶⁻⁷⁸

Given the severity and developmental onset of disease in animal models resulting from loss of HMGCS1, it is perhaps not surprising that the variants identified in patients do not dramatically impair HMGCS1 function. We suspect that biallelic loss-of-function variants in humans would cause prenatal lethality consistent with the anomalies observed in animal studies.⁷⁹ There are no individuals in gnomAD homozygous for loss-of-function HMGCS1 variants and only four individuals with heterozygous loss of function variants, supporting that HMGCS1 function is critical to life.

We have functionally investigated four of six HMGCS1 substitutions (S447P, Q29L, M70T and C268S) identified in our rigid spine syndrome cohort and showed no dramatic functional differences between the mutants and the wildtype. All mutants retained their 3D structure and dimerisation tendencies according to CD spectroscopy and size exclusion chromatography. These findings were similar to other studies of recombinant HMGCS1 mutants (p.C129A; *H. sapiens*⁸⁰ and p.A110G; *E. faecalis*⁵¹) showing no major difference in HMGCS1 structure or conformation. However, subtle albeit significant changes were detected by X-ray

crystallography.⁵¹ We thus speculate that the structural effect of the substitutions observed in our cohort (if any) may be partial and local, and therefore beyond the detection capacity of CD. Interestingly, comparison with an AcAc-CoA thiolase/HMGCS complex structure from *Methanothermococcus thermolithotrophicus* reveals that the residues equivalent to the Q29L, M70T and S447P substitutions are located on a region that interacts with a scaffold protein (Pfam DUF35).⁸¹ Disruption of such a complex in humans could further explain the effect of these mutations, however, no scaffold protein and ternary complex has yet been described for human AcAc-CoA thiolase/HMGCS.

We initially predicted that the HMGCS1 substitutions may impair HMGCS1 activity, given that HMGCS2 substitutions, including those distant from the catalytic site, have been associated with reduced enzymatic activity.⁷⁹ All four HMGCS1 mutants maintained enzymatic function within the same order of magnitude as the wildtype, including HMGCS1^{C268S} which harbours a substitution close to the active site. This mutant maintained ~70% of the activity of the wildtype. Of note, a superficial substitution in HMGCS2 p.R505Q (p.R468 in HMGCS1) has been associated with disease despite similarly retaining 70% of normal HMGCS2 activity.⁷⁹ Pathogenic substitutions in *GGPS1* have also been reported to have no significant impact on GGPS1 conformation and only mildly impaired enzyme activity *in vitro* and in patient-derived fibroblasts.¹¹ Similarly we see that hypomorphic variants in *HMGCS1* show activity levels similar to WT using *in vitro* assays. Some suggest that subtle changes in enzymatic function can lead to abnormal accumulation and processing of metabolites, causing dysregulated activities of other enzymes of the mevalonate pathway.^{56,72,82}

We have demonstrated that *HMGCS1* is expressed and detected in myoblasts, myotubes and skeletal muscle. Although enrichment of *HMGCS1* in the brain may suggest a neurological phenotype should result. *HMGCR* and *GGPS1* are also more abundant in brain tissue compared to skeletal muscle^{28,48-50} but have been predominantly associated with myopathic phenotypes.^{11,59,60,83-87} By western blotting, Hmgcs1 was similarly detected in mouse EDL and soleus muscle, suggesting that Hmgcs1 is similarly abundant in fast- and slow-twitch myofibres.

There are various hypotheses that suggest how disruptions to the mevalonate pathway cause skeletal muscle disease.^{20,88} These include alterations in the cholesterol abundance and fluidity of the sarcolemma, impaired mitochondrial function, and dysregulated isopentylation of selenocysteine-tRNA, which is required for *SELENON* expression.^{20,89,90} Of note, the clinical

resemblance between patients with *SELENON*-related and *HMGCS1*-related rigid spine syndrome, as well as other myopathies associated with the mevalonate pathway, may suggest dysregulated isopentenylation of selenocysteine-tRNA as a strong candidate pathomechanism.¹⁰ An alternative explanation to the muscle involvement may be associated with a dysregulation of isoenzymes of the mevalonate pathway exclusively expressed in skeletal muscle.^{91,92} For example, IDI2 (isopentenyl diphosphate isomerase 2; Supplementary Fig 4) is a skeletal muscle-specific isozyme of IDI1 which appears to be regulated by HMGCR abundance and activity.⁹² Statin inhibition of Hmgcr has been associated with significantly reduced *Idi2* mRNA levels in mouse skeletal muscle, whereas *Idi1* expression remained unaffected.⁹² This suggests that dysregulation of muscle-specific isoenzymes may differentially affect the mevalonate pathway in skeletal muscle compared to other tissue.⁹² Disruption of the mevalonate pathway, whether through statin inhibition⁹³ or mutation⁷⁵, also leads to mitochondrial abnormalities, consistent with the findings observed in *hmgcs1*^{-/-} zebrafish mutants. Interestingly, administration of mevalonic acid (the metabolite downstream of hmgcr) has been effective in treating HMGCR-myopathy in humans⁷⁵ and statin induced myopathy in mice.^{76,94,95} Overall, the disease mechanisms underlying the muscle phenotype may be clarified by multi-omic analyses as additional patients with mevalonate pathway-related myopathies are identified.⁹⁶

Conclusion

We report a novel autosomal recessive rigid spine syndrome we have termed *HMGCS1*-myopathy. We speculate that *HMGCS1* variants act by a hypomorphic mechanism, however, the precise cause of the myopathic phenotype in the patients remains to be elucidated. This report expands the genetic causes of rigid spine syndrome and highlights the mevalonate pathway as an essential pathway for muscle function. We encourage screening of *HMGCS1* in patients with molecularly unresolved rigid spine syndrome.

Acknowledgements

We would like to thank the patients and families for their participation in this study. We thank Dr. Amelie Nadeau and Dr. Katy Meilleur for their clinical expertise.

Funding

LNHD is supported by an Australian Government Research Training Program (RTP) Scholarship. GR (Investigator Grant, APP2007769), NGL (Fellowship APP1117510) and DS (Investigator Grant, APP2009732) are supported by the Australian NHMRC. This work is also supported by an NHMRC Ideas Grant (APP2002640). Sequencing and analysis of JPN1 were supported partly by Intramural Research Grant (2-5 and 5-6) for Neurological and Psychiatric Disorders of NCNP, and Japan Agency for Medical Research and Development under Grant Numbers 22ek0109490h0003. Sequencing and analysis of USA1 and USA2 were provided by the Broad Institute of MIT and Harvard Center for Mendelian Genomics (Broad CMG) and were funded by the National Human Genome Research Institute grants UM1 HG008900 and R01 HG009141 (with additional support from the National Eye Institute, and the National Heart, Lung and Blood Institute), and in part by grant number 2020-224274 from the Chan Zuckerberg Initiative DAF, an advised fund of Silicon Valley Community Foundation. The work in C.G. Bönnemann's laboratory is supported by intramural funds from the NIH National Institute of Neurological Disorders and Stroke.

Competing interests

The authors report no competing interests.

Supplementary material

Supplementary material is available online.

References

1. Neto OA, Tassy O, Biancalana V, Zanuteli E, Pourquié O, Laporte J. Integrative Data Mining Highlights Candidate Genes for Monogenic Myopathies. *PLoS One*. 2014;9(10):e110888.
2. Poewe W, Willeit H, Sluga E, Mayr U. The rigid spine syndrome--a myopathy of uncertain nosological position. *J Neurol Neurosurg Psychiatry*. 1985;48(9):887-893.
3. Ravenscroft G, Davis MR, Lamont P, Forrest A, Laing NG. New era in genetics of early-onset muscle disease: Breakthroughs and challenges. *Semin Cell Dev Biol*. 2017;64:160-170.

4. Kazamel M, Milone M. Congenital myopathy with a novel SELN missense mutation and the challenge to differentiate it from congenital muscular dystrophy. *J Clin Neurosci*. 2019;62:238-239.
5. Tordjman M, Dabaj I, Laforet P, et al. Muscular MRI-based algorithm to differentiate inherited myopathies presenting with spinal rigidity. *Eur Radiol*. 2018;28(12):5293-5303.
6. Goto I, Nagasaka S, Nagara H, Kuroiwa Y. Rigid spine syndrome. *J Neurol Neurosurg Psychiatry*. 1979;42(3):276-279.
7. Kayman-Kurekci G, Talim B, Korkusuz P, et al. Mutation in TOR1AIP1 encoding LAP1B in a form of muscular dystrophy: a novel gene related to nuclear envelopathies. *Neuromuscul Disord*. 2014;24(7):624-633.
8. Dai Y, Liang S, Huang Y, Chen L, Banerjee S. Targeted next generation sequencing identifies two novel mutations in SEPN1 in rigid spine muscular dystrophy 1. *Oncotarget*. 2016;7(51):83843-83849.
9. O'Grady GL, Best HA, Oates EC, et al. Recessive ACTA1 variant causes congenital muscular dystrophy with rigid spine. *Eur J Hum Genet*. 2015;23(6):883-886.
10. Moghadaszadeh B, Petit N, Jaillard C, et al. Mutations in SEPN1 cause congenital muscular dystrophy with spinal rigidity and restrictive respiratory syndrome. *Nat Genet*. 2001;29(1):17-18.
11. Foley AR, Zou Y, Dunford JE, et al. GGPS1 Mutations Cause Muscular Dystrophy/Hearing Loss/Ovarian Insufficiency Syndrome. *Ann Neurol* 2020;88(2):332-347.
12. Arbogast S, Beuvin M, Fraysse B, Zhou H, Muntoni F, Ferreiro A. Oxidative stress in SEPN1-related myopathy: from pathophysiology to treatment. *Ann Neurol*. 2009;65(6):677-686.
13. Koul R, Sankhla D, Al-Jahdhami S, et al. Rigid Spine Syndrome among Children in Oman. *Sultan Qaboos Univ Med J*. 2015;15(3):e364-369.
14. Quijano-Roy S, Mbieleu B, Bönnemann CG, et al. De novo LMNA mutations cause a new form of congenital muscular dystrophy. *Ann Neurol*. 2008;64(2):177-186.
15. Scoto M, Cullup T, Cirak S, et al. Nebulin (NEB) mutations in a childhood onset distal myopathy with rods and cores uncovered by next generation sequencing. *Eur J Hum Genet*. 2013;21(11):1249-1252.
16. Bharucha-Goebel DX, Santi M, Medne L, et al. Severe congenital RYR1-associated myopathy: the expanding clinicopathologic and genetic spectrum. *Neurology*. 2013;80(17):1584-1589.
17. Clarke NF, Kolski H, Dye DE, et al. Mutations in TPM3 are a common cause of congenital fiber type disproportion. *Ann Neurol*. 2008;63(3):329-337.
18. Chauveau C, Bonnemann CG, Julien C, et al. Recessive TTN truncating mutations define novel forms of core myopathy with heart disease. *Hum Mol Genet*. 2013;23(4):980-991.
19. Shalaby S, Hayashi YK, Goto K, et al. Rigid spine syndrome caused by a novel mutation in four-and-a-half LIM domain 1 gene (FHL1). *Neuromuscul Disord*. 2008;18(12):959-961.
20. Baker SK. Molecular clues into the pathogenesis of statin-mediated muscle toxicity. *Muscle Nerve*. 2005;31(5):572-580.
21. Yogev Y, Shorer Z, Koifman A, et al. Limb girdle muscular disease caused by HMGCR mutation and statin myopathy treatable with mevalonolactone. *Proc Natl Acad Sci U S A*. 2023;120(7):e2217831120.
22. Dubowitz V, Sewry CA, Oldfors A. *Muscle biopsy A Practical Approach*. Fifth edition. ed. London: Elsevier; 2020.

23. Pais LS, Snow H, Weisburd B, et al. seqr: A web-based analysis and collaboration tool for rare disease genomics. *Hum Mutat.* 2022;43(6):698-707.
24. Scala M, Nishikawa M, Ito H, et al. Variant-specific changes in RAC3 function disrupt corticogenesis in neurodevelopmental phenotypes. *Brain.* 2022;145(9):3308-3327.
25. Shafqat N, Turnbull A, Zschocke J, Oppermann U, Yue WW. Crystal Structures of Human HMG-CoA Synthase Isoforms Provide Insights into Inherited Ketogenesis Disorders and Inhibitor Design. *J Mol Biol.* 2010;398(4):497-506.
26. Burley SK, Berman HM, Bhikadiya C, et al. RCSB Protein Data Bank: biological macromolecular structures enabling research and education in fundamental biology, biomedicine, biotechnology and energy. *Nucleic Acids Res.* 2018;47(D1):D464-D474.
27. Wang J, Youkharibache P, Zhang D, et al. iCn3D, a web-based 3D viewer for sharing 1D/2D/3D representations of biomolecular structures. *Bioinformatics.* 2020;36(1):131-135.
28. Lizio M, Harshbarger J, Shimoji H, et al. Gateways to the FANTOM5 promoter level mammalian expression atlas. *Genome Biol.* 2015;16(1):22.
29. Anders S, Huber W. Differential expression analysis for sequence count data. *Genome Biol.* 2010;11(10):R106.
30. Yépez VA, Mertes C, Müller MF, et al. Detection of aberrant gene expression events in RNA sequencing data. *Nat Protoc.* 2021;16(2):1276-1296.
31. Yépez VA, Gusic M, Kopajtich R, et al. Clinical implementation of RNA sequencing for Mendelian disease diagnostics. *Genome Med.* 2022;14(1):38.
32. Brechtmann F, Mertes C, Matusevičiūtė A, et al. OUTRIDER: A Statistical Method for Detecting Aberrantly Expressed Genes in RNA Sequencing Data. *Am J Hum Genet.* 2018;103(6):907-917.
33. Dofash LNH, Monahan G, Servián-Morilla E, et al. A *KLHL40* 3' UTR splice-altering variant causes milder NEM8, an under-appreciated disease mechanism. *medRxiv.* 2022:2022.2008.2008.22278402.
34. Vandesompele J, De Preter K, Pattyn F, et al. Accurate normalization of real-time quantitative RT-PCR data by geometric averaging of multiple internal control genes. *Genome Biol.* 2002;3(7):research0034.0031.
35. McNamara EL, Taylor RL, Clayton JS, et al. Systemic AAV8-mediated delivery of a functional copy of muscle glycogen phosphorylase (Pygm) ameliorates disease in a murine model of McArdle disease. *Hum Mol Genet.* 2020;29(1):20-30.
36. Dofash LNH, Monahan GV, Servián-Morilla E, et al. A *KLHL40* 3' UTR splice-altering variant causes milder NEM8, an under-appreciated disease mechanism. *Hum Mol Genet.* 2022.
37. Schneider CA, Rasband WS, Eliceiri KW. NIH Image to ImageJ: 25 years of image analysis. *Nat Methods.* 2012;9(7):671-675.
38. Goullée H, Taylor RL, Forrest ARR, Laing NG, Ravenscroft G, Clayton JS. Improved CRISPR/Cas9 gene editing in primary human myoblasts using low confluency cultures on Matrigel. *Skelet Muscle.* 2021;11(1).
39. Tucker EJ, Baker MJ, Hock DH, et al. Premature Ovarian Insufficiency in CLPB Deficiency: Transcriptomic, Proteomic and Phenotypic Insights. *J Clin Endocrinol Metab.* 2022;107(12):3328-3340.
40. Froger A, Hall JE. Transformation of plasmid DNA into E. coli using the heat shock method. *J Vis Exp.* 2007(6):253.
41. Haywood J, Schmidberger JW, James AM, et al. Structural basis of ribosomal peptide macrocyclization in plants. *eLife.* 2018;7:e32955.

42. Wilkins MR GE, Bairoch A, Sanchez JC, Williams KL, Appel RD, et al. Protein identification and analysis tools in the ExPASy server. *Methods Mol Biol.* 1999;531-552.
43. Lowe DM, Tubbs PK. 3-Hydroxy-3-methylglutaryl-coenzyme A synthase from ox liver. Properties of its acetyl derivative. *Biochem J.* 1985;227(2):601-607.
44. Horstick EJ, Jordan DC, Bergeron SA, et al. Increased functional protein expression using nucleotide sequence features enriched in highly expressed genes in zebrafish. *Nucleic acids research.* 2015;43(7):e48.
45. Hua Y, Laserstein P, Helmstaedter M. Large-volume en-bloc staining for electron microscopy-based connectomics. *Nature Communications.* 2015;6(1):7923.
46. Schindelin J, Arganda-Carreras I, Frise E, Frise E, Kaynig V, et al. Fiji: an open-source platform for biological-image analysis. 2012(1548-7105 (Electronic)).
47. Yu J, Deng J, Guo X, et al. The GGC repeat expansion in NOTCH2NLC is associated with oculopharyngodistal myopathy type 3. *Brain.* 2021;144(6):1819-1832.
48. Fagerberg L, Hallström BM, Oksvold P, et al. Analysis of the human tissue-specific expression by genome-wide integration of transcriptomics and antibody-based proteomics. *Mol Cell Proteomics.* 2014;13(2):397-406.
49. Consortium GT. The Genotype-Tissue Expression (GTEx) project. *Nat Genet.* 2013;45(6):580-585.
50. Uhlén M, Fagerberg L, Hallström BM, et al. Proteomics. Tissue-based map of the human proteome. *Science.* 2015;347(6220):1260419.
51. Steussy CN, Robison AD, Tetrick AM, et al. A structural limitation on enzyme activity: the case of HMG-CoA synthase. *Biochemistry.* 2006;45(48):14407-14414.
52. Sztal TE, Ruparelia AA, Williams C, Bryson-Richardson RJ. Using Touch-evoked Response and Locomotion Assays to Assess Muscle Performance and Function in Zebrafish. LID - 10.3791/54431 [doi] LID - 54431. 2016(1940-087X (Electronic)).
53. Lee T, Takami Y, Yamada K, et al. A Japanese case of mitochondrial 3-hydroxy-3-methylglutaryl-CoA synthase deficiency who presented with severe metabolic acidosis and fatty liver without hypoglycemia. *JIMD Rep.* 2019;48(1):19-25.
54. Thompson GN, Hsu BY, Pitt JJ, Treacy E, Stanley CA. Fasting hypoketotic coma in a child with deficiency of mitochondrial 3-hydroxy-3-methylglutaryl-CoA synthase. *N Engl J Med.* 1997;337(17):1203-1207.
55. Rojnueangnit K, Maneechai P, Thaweekul P, et al. Expanding phenotypic and mutational spectra of mitochondrial HMG-CoA synthase deficiency. *Eur J Med Genet.* 2020;63(12):104086.
56. McLarren KW, Severson TM, du Souich C, et al. Hypomorphic temperature-sensitive alleles of NSDHL cause CK syndrome. *Am J Hum Genet.* 2010;87(6):905-914.
57. du Souich C, Chou A, Yin J, et al. Characterization of a new X-linked mental retardation syndrome with microcephaly, cortical malformation, and thin habitus. *Am J Med Genet A.* 2009;149A(11):2469-2478.
58. Grange DK, Kratz LE, Braverman NE, Kelley RI. CHILD syndrome caused by deficiency of 3beta-hydroxysteroid-delta8, delta7-isomerase. *Am J Med Genet.* 2000;90(4):328-335.
59. Mohassel P, Mammen AL. Anti-HMGCR Myopathy. *J Neuromuscul Dis.* 2018;5(1):11-20.
60. Mammen AL, Chung T, Christopher-Stine L, et al. Autoantibodies against 3-hydroxy-3-methylglutaryl-coenzyme A reductase in patients with statin-associated autoimmune myopathy. *Arthritis Rheum.* 2011;63(3):713-721.

61. Kishi T, Rider LG, Pak K, et al. Association of Anti-3-Hydroxy-3-Methylglutaryl-Coenzyme A Reductase Autoantibodies With DRB1*07:01 and Severe Myositis in Juvenile Myositis Patients. *Arthritis Care Res (Hoboken)*. 2017;69(7):1088-1094.
62. Porter FD, Herman GE. Malformation syndromes caused by disorders of cholesterol synthesis. *J Lipid Res*. 2011;52(1):6-34.
63. Peciuliene S, Burnyte B, Gudaitiene R, et al. Perinatal manifestation of mevalonate kinase deficiency and efficacy of anakinra. *Pediatr Rheumatol Online J*. 2016;14(1):19.
64. Gibson KM, Hoffmann G, Nyhan WL, et al. Mevalonate kinase deficiency in a child with cerebellar ataxia, hypotonia and mevalonic aciduria. *European Journal of Pediatrics*. 1988;148(3):250-252.
65. Morales-Rosado JA, Schwab TL, Macklin-Mantia SK, et al. Bi-allelic variants in HMGCR cause an autosomal-recessive progressive limb-girdle muscular dystrophy. *Am J Hum Genet*. 2023;110(6):989-997.
66. Tiniakou E, Pinal-Fernandez I, Lloyd TE, et al. More severe disease and slower recovery in younger patients with anti-3-hydroxy-3-methylglutaryl-coenzyme A reductase-associated autoimmune myopathy. *Rheumatology (Oxford)*. 2017;56(5):787-794.
67. Ghaoui R, Cooper ST, Lek M, et al. Use of Whole-Exome Sequencing for Diagnosis of Limb-Girdle Muscular Dystrophy: Outcomes and Lessons Learned. *JAMA Neurol*. 2015;72(12):1424-1432.
68. Badayan I, Cudkowicz ME. Profound Muscle Weakness and Pain after One Dose of Actonel. *Case Reports in Medicine*. 2009;2009:693014.
69. DeMonaco HJ. Patient- and Physician-Oriented Web Sites and Drug Surveillance: Bisphosphonates and Severe Bone, Joint, and Muscle Pain. *Arch Intern Med*. 2009;169(12):1164-1166.
70. Kaiyrzhanov R, Perry L, Rocca C, et al. GGPS1-associated muscular dystrophy with and without hearing loss. *Ann Clin Transl Neurol*. 2022;9(9):1465-1474.
71. Sapir A, Tsur A, Koorman T, et al. Controlled sumoylation of the mevalonate pathway enzyme HMGS-1 regulates metabolism during aging. *Proc Natl Acad Sci U S A*. 2014;111(37):E3880-3889.
72. Woollett LA. Where does fetal and embryonic cholesterol originate and what does it do? *Annu Rev Nutr*. 2008;28:97-114.
73. Bagheri-Fam S, Chen H, Wilson S, et al. The gene encoding the ketogenic enzyme HMGCS2 displays a unique expression during gonad development in mice. *PLoS One*. 2020;15(1):e0227411.
74. Dickinson ME, Flenniken AM, Ji X, et al. High-throughput discovery of novel developmental phenotypes. *Nature*. 2016;537(7621):508-514.
75. Ranji P, Rauthan M, Pitot C, Pilon M. Loss of HMG-CoA reductase in *C. elegans* causes defects in protein prenylation and muscle mitochondria. 2014(1932-6203 (Electronic)).
76. Eisa-Beygi S, Hatch G, Noble S, Ekker M, Moon TW. The 3-hydroxy-3-methylglutaryl-CoA reductase (HMGCR) pathway regulates developmental cerebral-vascular stability via prenylation-dependent signalling pathway. *Developmental Biology*. 2013;373(2):258-266.
77. Xiang Z, Reeves SA. Simvastatin induces cell death in a mouse cerebellar slice culture (CSC) model of developmental myelination. *Exp Neurol*. 2009;215(1):41-47.
78. Signore IA, Jerez C, Figueroa D, et al. Inhibition of the 3-hydroxy-3-methyl-glutaryl-CoA reductase induces orofacial defects in zebrafish. *Birth Defects Res A Clin Mol Teratol*. 2016;106(10):814-830.

79. Puisac B, Marcos-Alcalde I, Hernández-Marcos M, et al. Human Mitochondrial HMG-CoA Synthase Deficiency: Role of Enzyme Dimerization Surface and Characterization of Three New Patients. *Int J Mol Sci.* 2018;19(4):1010.
80. Rokosz LL, Boulton DA, Butkiewicz EA, et al. Human cytoplasmic 3-hydroxy-3-methylglutaryl coenzyme A synthase: expression, purification, and characterization of recombinant wild-type and Cys129 mutant enzymes. *Arch Biochem Biophys.* 1994;312(1):1-13.
81. Vögeli B, Engilberge S, Girard E, et al. Archaeal acetoacetyl-CoA thiolase/HMG-CoA synthase complex channels the intermediate via a fused CoA-binding site. *Proc Natl Acad Sci U S A.* 2018;115(13):3380-3385.
82. Houten SM, Frenkel J, Rijkers GT, Wanders RJ, Kuis W, Waterham HR. Temperature dependence of mutant mevalonate kinase activity as a pathogenic factor in hyper-IgD and periodic fever syndrome. *Hum Mol Genet.* 2002;11(25):3115-3124.
83. Westwood FR, Scott RC, Marsden AM, Bigley A, Randall K. Rosuvastatin: characterization of induced myopathy in the rat. *Toxicol Pathol.* 2008;36(2):345-352.
84. Yablonka-Reuveni Z. The skeletal muscle satellite cell: still young and fascinating at 50. *J Histochem Cytochem.* 2011;59(12):1041-1059.
85. Feng X, Naz F, Juan AH, Dell'Orso S, Sartorelli V. Identification of Skeletal Muscle Satellite Cells by Immunofluorescence with Pax7 and Laminin Antibodies. *J Vis Exp.* 2018(134).
86. Grunwald SA, Popp O, Haafke S, et al. Statin-induced myopathic changes in primary human muscle cells and reversal by a prostaglandin F2 alpha analogue. *Sci Rep.* 2020;10(1):2158.
87. Trapani L, Segatto M, La Rosa P, et al. 3-hydroxy 3-methylglutaryl coenzyme a reductase inhibition impairs muscle regeneration. *J Cell Biochem.* 2012;113(6):2057-2063.
88. Ahmadi Y, Ghorbanihaghjo A, Naghi-Zadeh M, Yagin NL. Oxidative stress as a possible mechanism of statin-induced myopathy. *Inflammopharmacology.* 2018;26(3):667-674.
89. Moosmann B, Behl C. Selenoproteins, Cholesterol-Lowering Drugs, and the Consequences Revisiting of the Mevalonate Pathway. *Trends Cardiovasc Med.* 2004;14(7):273-281.
90. Kromer A, Moosmann B. Statin-Induced Liver Injury Involves Cross-Talk between Cholesterol and Selenoprotein Biosynthetic Pathways. *Mol Pharmacol.* 2009;75(6):1421-1429.
91. Huang J, Du J, Lin W, et al. Regulation of lactate production through p53/ β -enolase axis contributes to statin-associated muscle symptoms. *EBioMedicine.* 2019;45:251-260.
92. Clizbe DB, Owens ML, Masuda KR, Shackelford JE, Krisans SK. IDI2, a second isopentenyl diphosphate isomerase in mammals. *J Biol Chem.* 2007;282(9):6668-6676.
93. Mollazadeh H, Tavana E, Fanni G, et al. Effects of statins on mitochondrial pathways. *Journal of Cachexia, Sarcopenia and Muscle.* 2021;12(2):237-251.
94. Chen JA-O, Niu X, King MJ, Noedl MT, Tabin CJ, Galloway JA-O. The mevalonate pathway is a crucial regulator of tendon cell specification. LID - 10.1242/dev.185389 [doi] LID - dev185389. 2020(1477-9129 (Electronic)).
95. Thorpe JL, Doitsidou M, Ho S-Y, Raz E, Farber SA. Germ Cell Migration in Zebrafish Is Dependent on HMGCoA Reductase Activity and Prenylation. *Developmental Cell.* 2004;6(2):295-302.

96. Coman D, Vissers LELM, Riley LG, et al. Squalene Synthase Deficiency: Clinical, Biochemical, and Molecular Characterization of a Defect in Cholesterol Biosynthesis. *Am J Hum Genet.* 2018;103(1):125-130.

Figure legends

Figure 1 HMGCS1-myopathy cohort. (A) Pedigrees of the four families with biallelic variants in *HMGCS1* segregating with rigid spine syndrome.

Figure 2 Muscle MRI and pathology associated with HMGCS1-myopathy. (A) Muscle MRI performed for Patient P1 (SPA1) (i-iii) and Patient P4 (ITA1) during adulthood (iv-vi). Variation in T1 signal indicative of fatty replacement in the posterior muscles of the cervical paraspinal muscles (stars) (i), the posterior compartment of the thigh (arrows) (ii, iv, v), and the posterior compartment of the leg (arrows) (vi). Evidence of edema in the posterior compartment of the thighs in Patient P1 shown by STIR (arrows) (iii). Vastus intermedius is also affected to a lesser extent (arrow heads). (B) Light microscopy staining of muscle biopsies from patients P1 (SPA1) during teenagerhood (top panel), P3 (JPN1) during childhood and adulthood (middle panels), and P4 (ITA1) during childhood (bottom panel). Haematoxylin & Eosin (H&E) and Gömöri Trichrome (GT) staining show occasional internal nuclei and rimmed vacuoles in some patients. Succinate dehydrogenase (SDH) staining of SPA1 and nicotinamide adenine dinucleotide (NADH) staining of JPN1 and ITA1 patient biopsies reveal irregularities in staining including moth-eaten appearances and core-like regions (arrows). Scale bars represent 20 μm or 50 μm as indicated.

Figure 3 HMGCS1 variants. (A) Schematic representations of the *HMGCS1* gene (top) and protein (bottom) linear architectures. The *HMGCS1* gene includes untranslated regions (empty boxes), coding exons (filled boxes) and introns (horizontal line). Variants identified in patients with rigid spine syndrome are labelled, including both missense (circle) and truncating (triangle) variants. The variants are coloured according to the families they have been identified in (red: JPN1, blue: USA1, green: ITA1, orange: SPA1). Letters A, B and s within the protein structure (bottom) respectively represent residues of the active site (E95, C129, H264), coenzyme A binding site (N167, S221, K269, K273) and salt bridge (D119, E121, R194, D208, K239, K461 and H462). Diagram not to scale. (B) Conservation of the six missense variant positions in various species and in HMGCS2; the mitochondrial paralogue. Asterisks indicate complete conservation of residues in the analysed species. (C) RNA-seq fold change in

HMGCS1 expression in patient P3 (JPN1) compared to three unaffected controls (left). Error bars correspond to standard deviation. RNA-seq reads indicate virtually monoallelic expression of *HMGCS1* c.86A>T, p.(Q29L) suggesting the c.344_345del, p.(S115Wfs*12) variant undergoes nonsense mediated decay (right figure). **(D)** Visualisation of the HMGCS1 dimer (PDB: 2P8U) using PyMOL. HMGCS1 chain A (right) represented by a ribbon and chain B (left) shown as a cartoon. Ac-CoA represented as dark grey spheres. Variant positions (represented by licorice sticks) coloured by family. Close-up representation showing the minimum distance between S447 and Q29 is ~ 4.3 Å (dashed box).

Figure 4 *HMGCS1* is expressed in various tissues including patient skeletal muscle. **(A)** Quantitative real-time PCR analysis using cDNA from healthy human cell lines and tissues. Expression data from human embryonic kidney cells (HEK293FT cell line), fibroblasts, myoblasts (D0), myotubes at D2, D4, D6, D8 of differentiation, cortex, skeletal muscle controls from *in vitro* contractile testing and fetal muscle. Transcript levels were normalised to the geometric mean of *EEF2* and *TBP* using the delta Ct method. Data presented as mean \pm SEM ($n=2-7$ biological). **(B)** Graphical presentation of HMGCS1 peptides detected by quantitative mass spectrometry from myoblasts (MB) and myotubes at day 2 (D2) and day 8 (D8) of differentiation. **(C-F)** Western blotting for HMGCS1 (top panels) in **(C)** primary human (Cook Myosite) myoblasts and myotubes from days 0-12 of differentiation, in **(D)** control human tissue and cell lines, and in **(E)** patient P1 (SPA1) skeletal muscle alongside healthy skeletal muscle controls. Recombinant wildtype HMGCS1 (Rec. HMGCS1) used as a control for antibody specificity. **(F)** Western blotting for HMGCS1 in mouse *extensor digitorum longus* (EDL) and soleus muscles (top panel). Western blots for GAPDH and gel-stained myosin heavy chain (MHC) bands are shown to demonstrate comparable loading of total and muscle proteins.

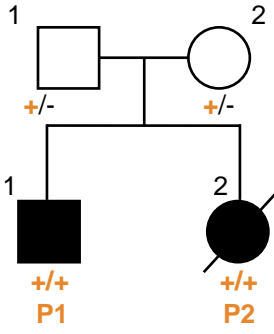
Figure 5 Circular dichroism analyses of recombinant wildtype and mutant HMGCS1. **(A-D)** Circular dichroic spectra scans (195-260 nm) of wildtype and mutant HMGCS1 (0.1 mg/mL) measured at **(A)** 15°C, **(B)** 25°C, **(C)** 55°C and **(D)** 95°C in buffer containing 10 mM sodium phosphate buffer pH 7.4, (including 1% of original protein buffer: 150 mM NaCl, 50 mM Tris and 10% glycerol). **(E)** Representative melting curves of wildtype and mutant HMGCS1 (0.1 mg/mL) measured at 229 nm. Melting curves (37-55°C) were fitted to sigmoidal logistic regression four parameter fits where the IC50 (point of inflection) were taken as the melting temperatures (T_m) plotted in **(F)**, data ($n=4-7$) presented as mean \pm SEM.

Figure 6 *hmgcs1*^{-/-} zebrafish have severe mitochondrial abnormalities and an early lethal phenotype. (A) Brightfield images of wildtype and *hmgcs1*^{-/-} embryos at 48 hours post fertilisation (hpf). *hmgcs1*^{-/-} embryos have developmental delay, reduced pigmentation, blood pooling in the brain. (B) Quantification of movement to a touch- evoke assay. *hmgcs1*^{-/-} embryos lack a movement response to touch, unlike wildtype and heterozygous siblings. Injection of mRNA encoding HMGCS1 rescues the movement defects in *hmgcs1*^{-/-} embryos. (C) Survival assay on the progeny of a *hmgcs1*^{+/-} in cross. In control injected fish only 79% survived until day 4 and no *hmgcs1*^{-/-} fish were detected at this time, as indicated in brackets, demonstrating that loss of Hmgcs1 results in early embryo lethality. Injection of *HMGCS1* mRNA rescues the lethality in *hmgcs1*^{-/-} embryos, with 100% of injected fish surviving until day 4, and subsequent genotyping indicating 33% of the fish were *hmgcs1*^{-/-}. 24 embryos from the *hmgcs1*^{+/-} in cross were used for each assay. (D) Scanning electron microscopy images of longitudinal muscle sections at 48hpf, demonstrating mitochondria associated with skeletal muscle. *hmgcs1*^{-/-} embryos have an increased proportion of mitochondria with detached membranes. Magenta arrows indicate mitochondria, cyan arrows indicate myofibres. Scale bar represents 1 μ m. (E) Mitochondrial density is not affected in *hmgcs1*^{-/-} embryo skeletal muscle (students t-test). (F) The proportion of mitochondria with detached membranes is higher in *hmgcs1*^{-/-} embryos compared to wildtype (Fisher's exact test). Statistics were performed in Prism 9 (GraphPad). Statistically significant differences are indicated on the graphs by the p-value.

A

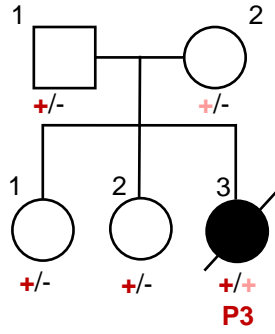
SPA1

c.1339T>C: p.(S447P)



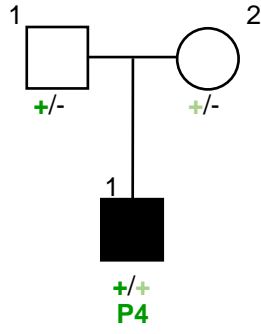
JPN1

c.344_345del:p.(S115Wfs*12)
c.86A>T:p.(Q29L)



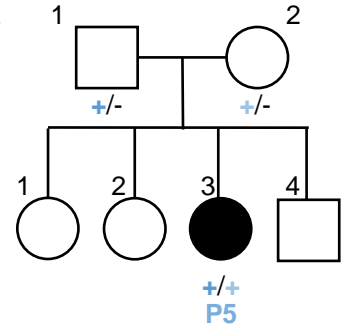
ITA1

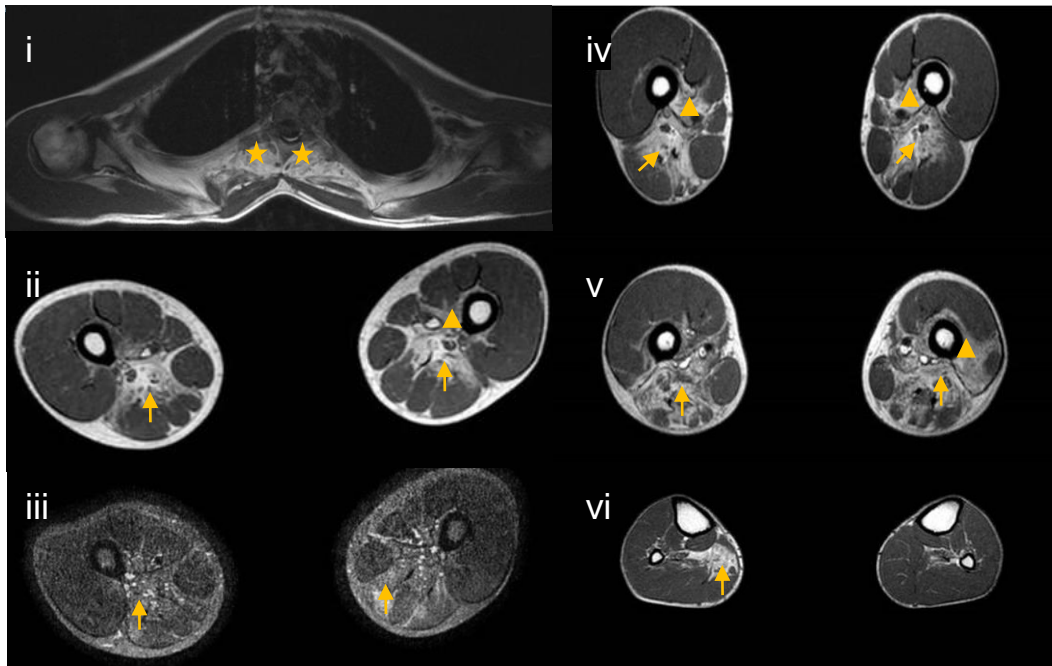
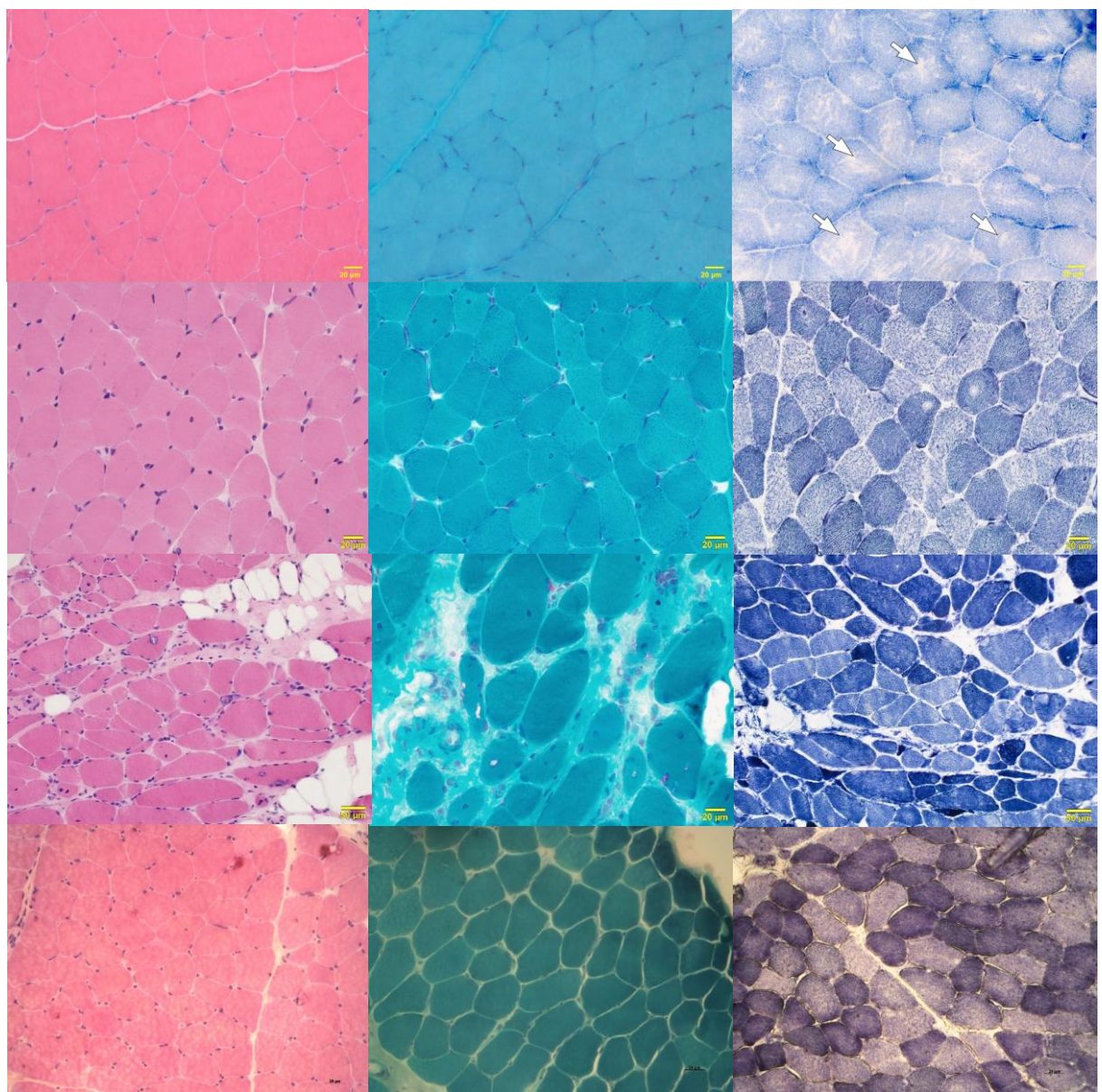
c.1289G>A: p.(R430K)
c.890G>T: p.(G297V)



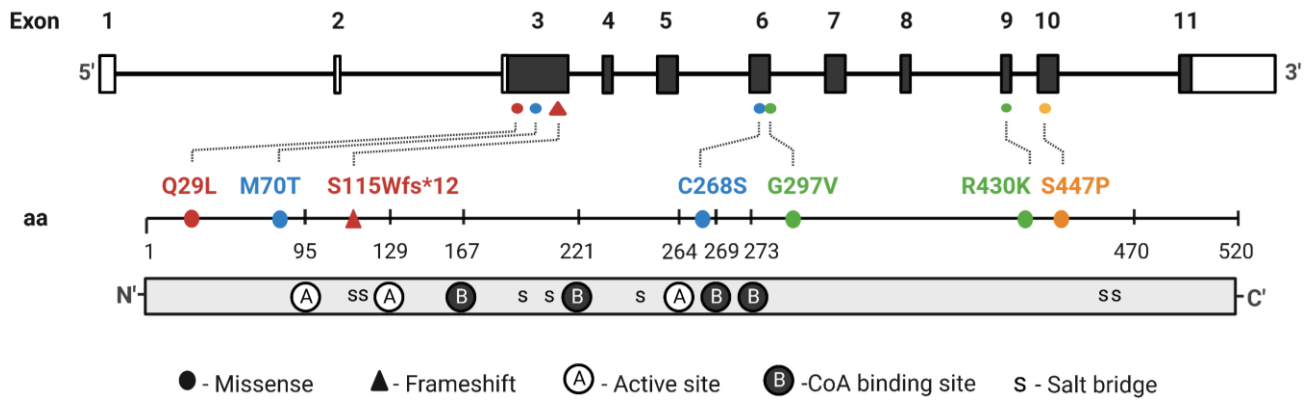
USA1

c.803G>C: (p.C268S)
c.209T>C: (p.M70T)



A**SPA1****ITA1****B****H&E****GT****SDH / NADH****SPA1****JPN1****JPN1****ITA1**

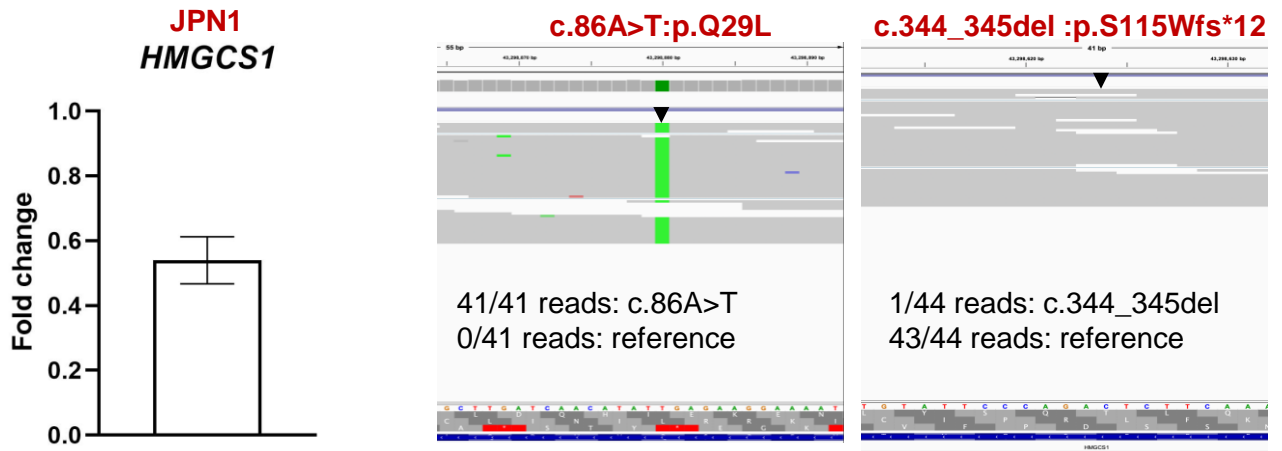
A



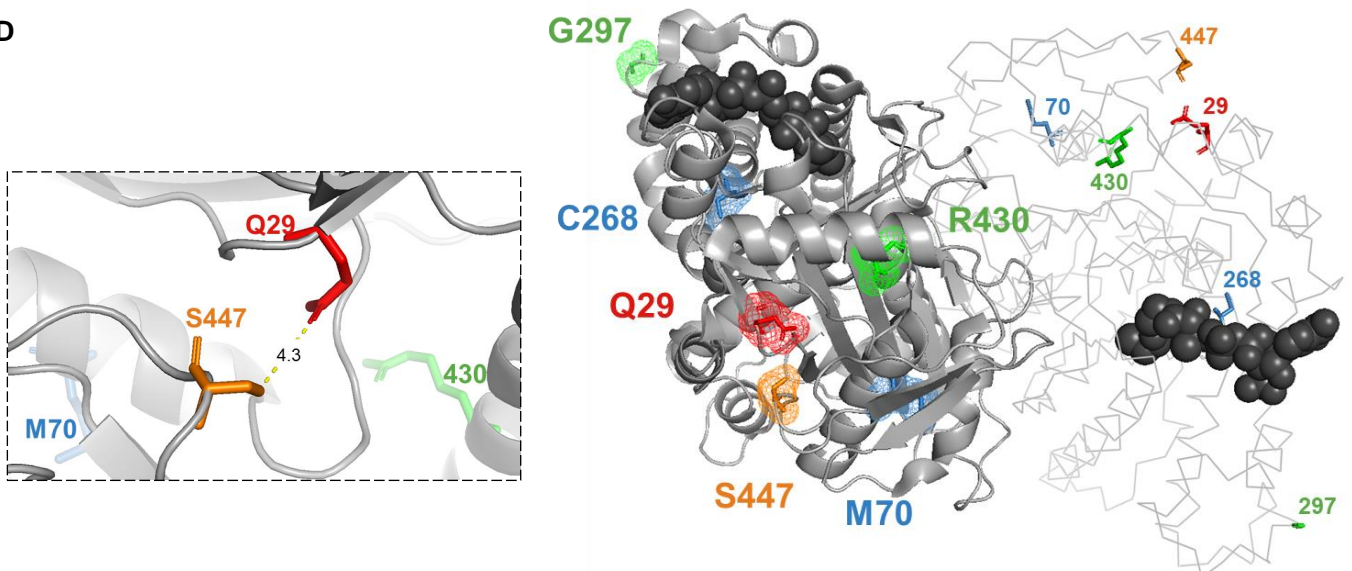
B

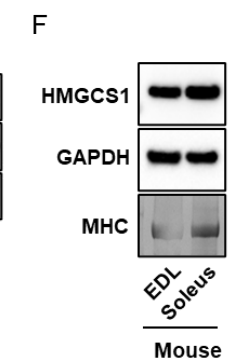
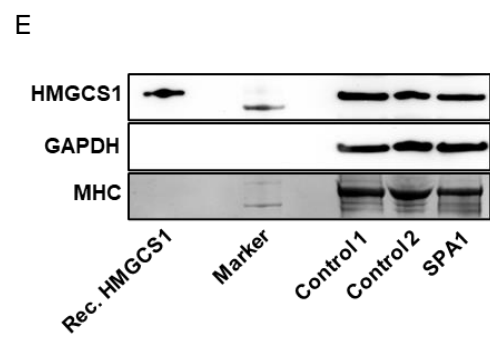
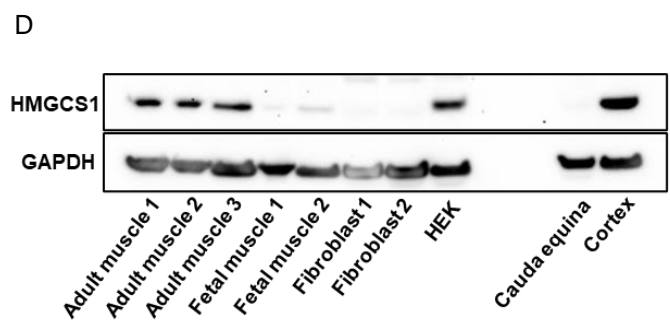
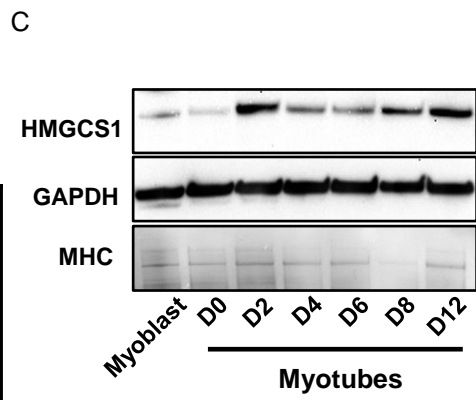
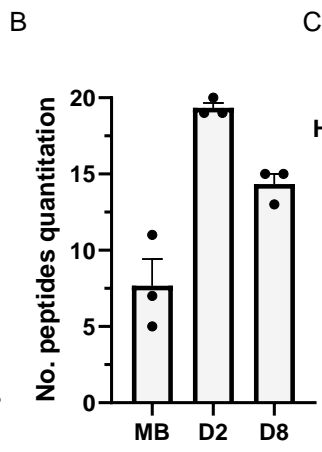
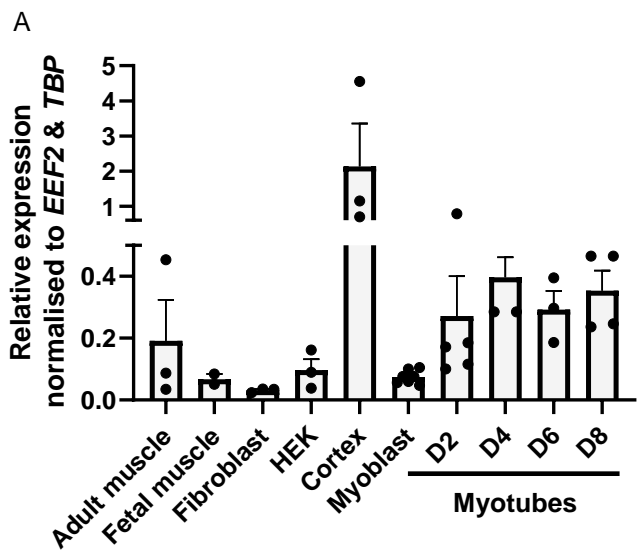
	Q29L	M70T	C268S	G297V	R430K	S447P
Q01581 HMCS1_HUMAN	IYFPS L YVD	INSLC T TVV	HSPY S KLVQK	IY S VLEAFG	MKL K EDTH	SID P LFEG
P54868 HMCS2_HUMAN	IYFPSQYVD	INSLCMTVV	HSPYCKLVQK	IYSGLEAFG	MKLREDTH	SIDSLFEG
P17425 HMCS1_RAT	IYFPSQYVD	INSLCLTVV	HSPYCKLVQK	IYSGLEAFG	MKLREDTH	SIDSLFEG
Q8JZK9 HMCS1_MOUSE	IYFPSQYVD	INSLCLTVV	HSPYCKLVQK	IYSGLEAFG	MKLREDTH	SIDSLFEG
P23228 HMCS1_CHICK	IYFPSQYVD	INSLCLTVV	HSPYCKLVQK	GVFSGLEAF	MKIRQETH	SVEDLFEG
P13704 HMCS1_CRIGR	IYFPSQYVD	INSLCLTVV	HSPYCKLVQK	IYSGLEAFG	MKLREDTH	SIDSLFEG
Q5R7Z9 HMCS1_PONAB	IYFPSQYVD	INSLCMTVV	HSPYCKLVQK	IYSGLEAFG	MKLREDTH	SIDSLFEG
P54961 HMCS1_BLAG	LIFPSQYVD	INSLCLTVV	HAPYCKLVQK	KYSSLEALK	METREHNN	SIDVLFPG
	** * ****	***** **	* * * * *	*	* *	** *

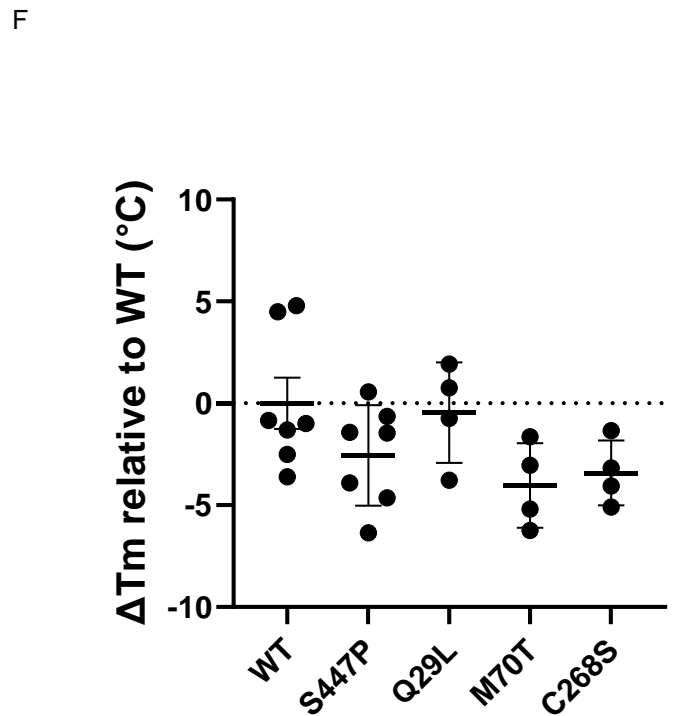
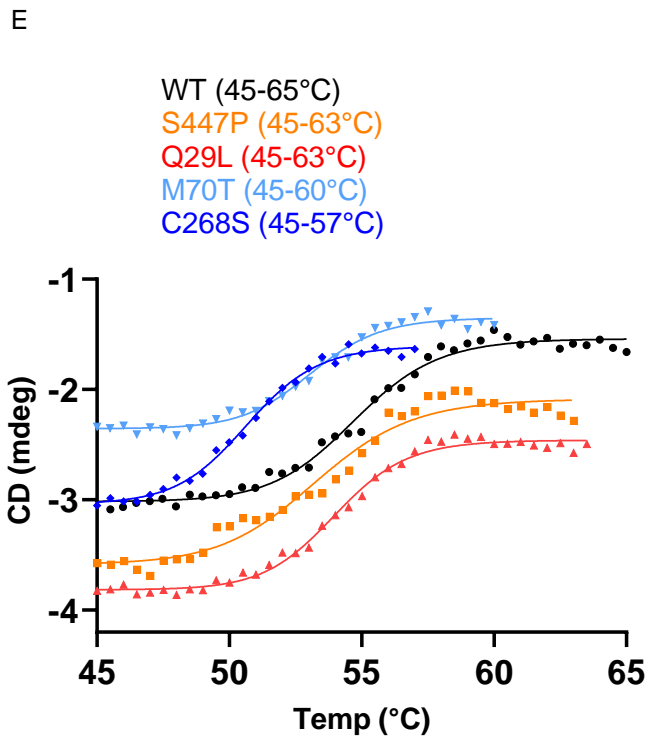
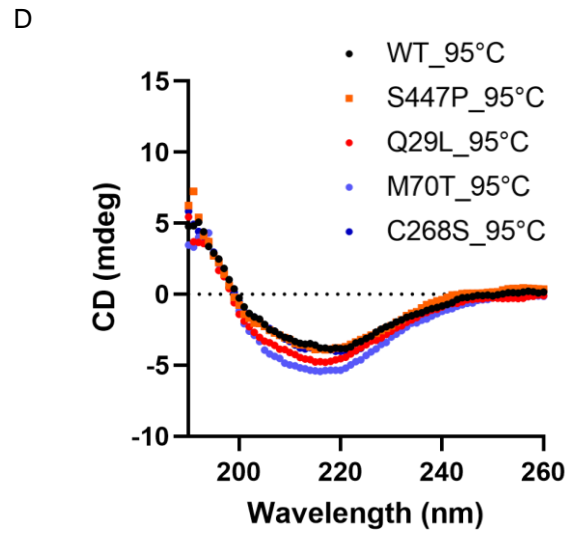
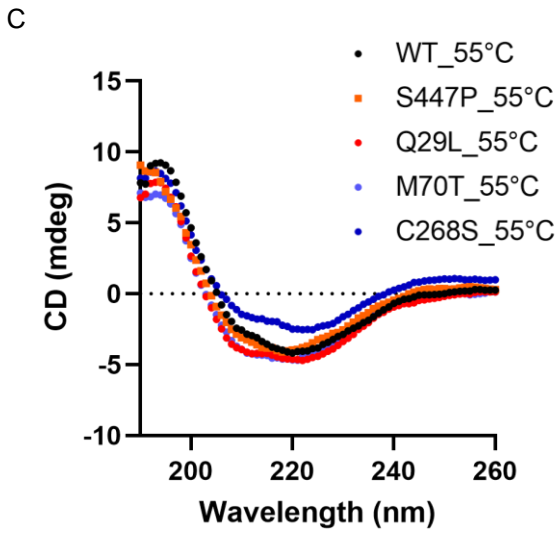
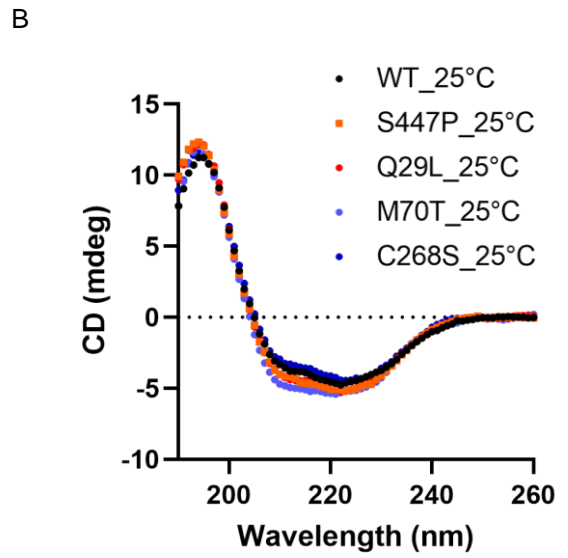
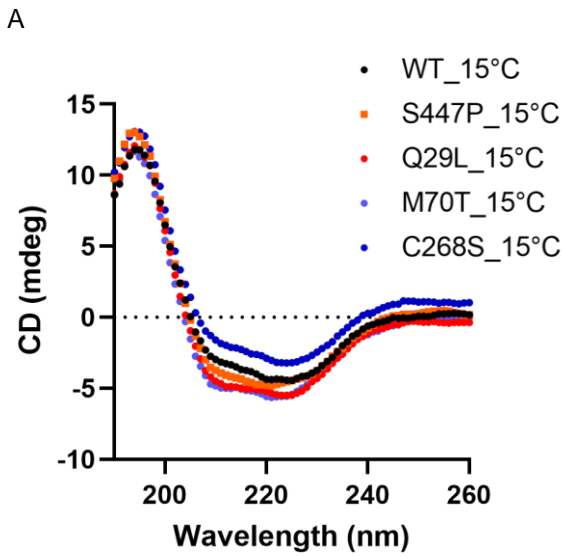
C



D







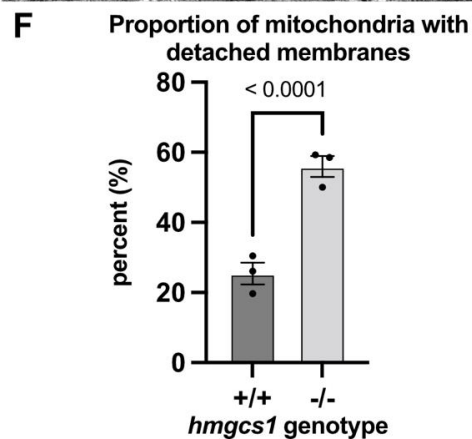
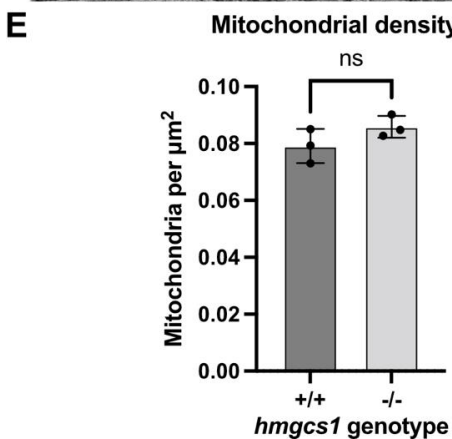
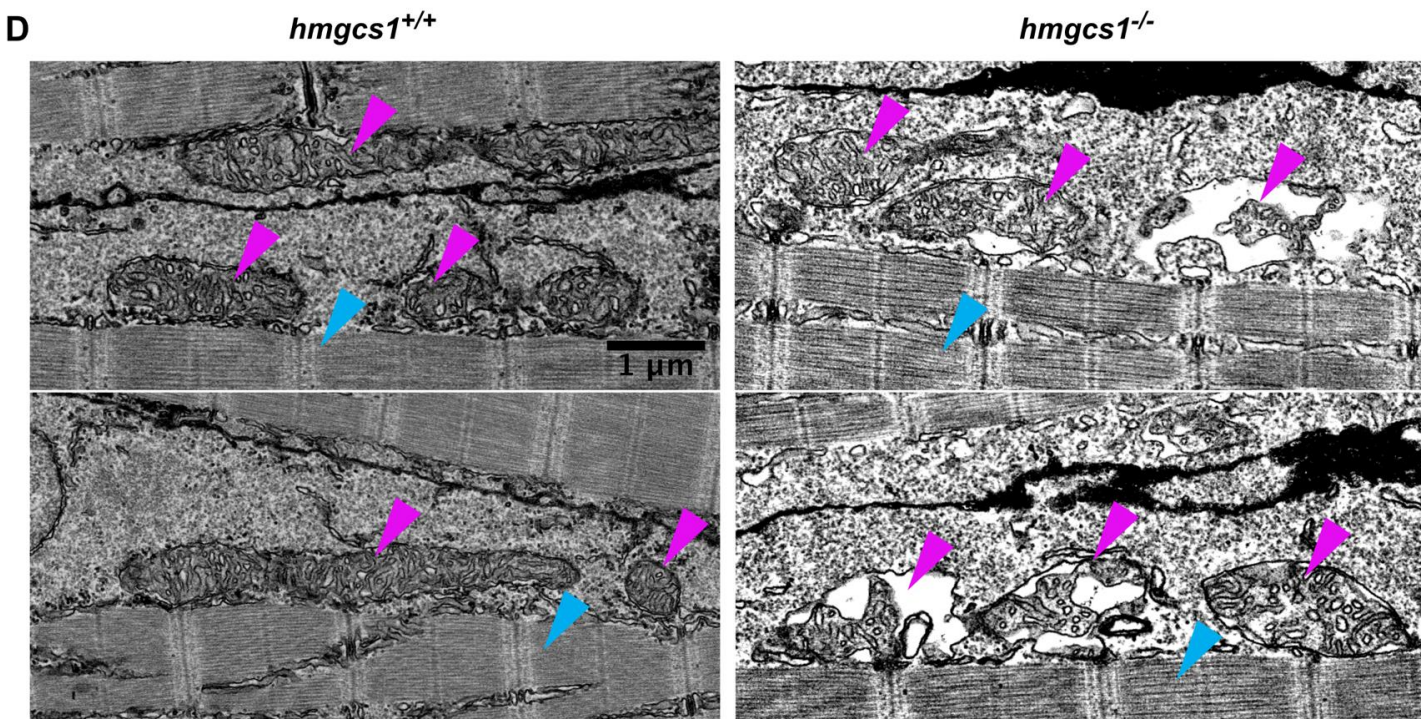
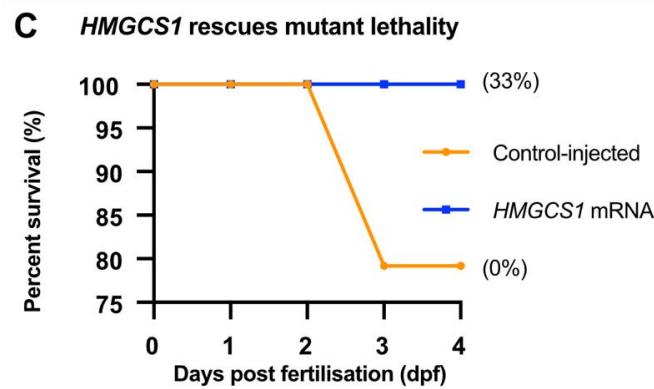
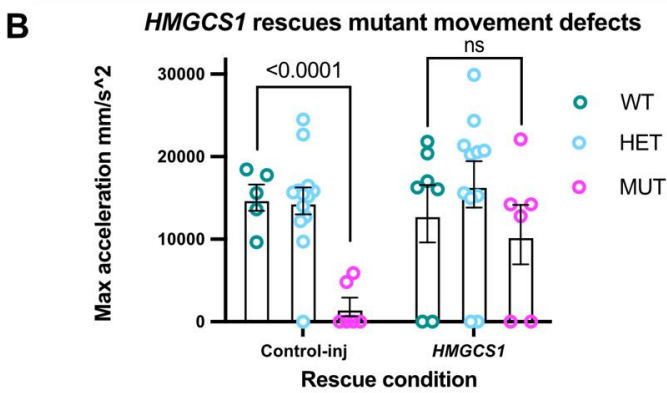
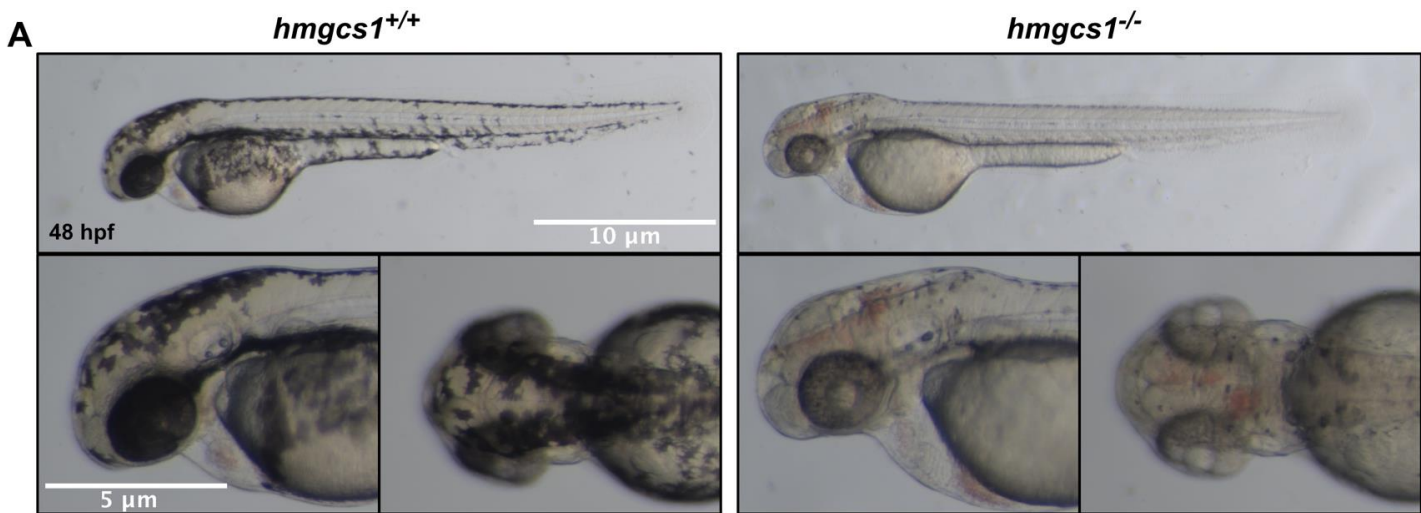


Table 1 Clinical summary of the HMGCS1-myopathy cohort

Family	SPA I		JPN I	ITA I	USA I
Patient	P1	P2	P3	P4	P5
Sex	M	F	F	M	F
Onset (yo)	childhood	childhood	childhood	childhood	birth
Age at death (yo)	alive	teenage years	adulthood	alive	alive
Cause of death	n/a	Respiratory failure	Acute exacerbation of psychosis with delusion	n/a	n/a
Age at last FU (yo)	adulthood	teenage years	adulthood	adulthood	adulthood
Proximal limb weakness	Yes	No	Yes	Yes	Yes
Distal limb weakness	No	No	Yes (mild)	Yes (mild)	Yes (mild)
Facial weakness	No	No	No	No	No
Bulbar weakness	No	No	No	No	Yes
Scapular winging	Yes	Yes	Yes	Yes	No
Rigid spine, dorsolumbar	Yes	Yes	Yes	Yes	Yes
Rigid spine, cervical	Yes	Yes	Yes	Yes	Yes
Scoliosis	Yes	Yes	Yes	Yes	Yes
Ophthalmoparesis	No	No	No	No	No
Ptosis	No	No	No	No	No
Muscle MRI	Yes	No	Yes	Yes	No
CK (IU/L)	190-7,890	430-4,100	400-2,000	274-939	200-5,000
Cardiac involvement	No	No	LVEF 57%	LVEF 55-60%	No
Pulmonary function test	Restrictive FVC, 1.51 L (37%)	Restrictive FVC, 56%	FVC 440 mL (16%)	Restrictive: FVC 1.11 L (26% pred)	Restrictive FVC, 10%
Episodic worsening during intercurrent disease	No	Yes	Yes	No	No